Flight data analysis of the BERM radiation monitor aboard the BepiColombo mission to Mercury

Carlota Patrícia Donga Cardoso

Thesis to obtain the Master of Science Degree in

Engineering Physics

Supervisors: Prof. Patrícia Carla Serrano Gonçalves
Dr. Marco Gui Alves Pinto

Examination Committee

Chairperson: Prof. Name of the Chairperson
Supervisor: Prof. Patrícia Carla Serrano Gonçalves
Members of the Committee: Prof. Name of First Committee Member
Dr. Name of Second Committee Member
Eng. Name of Third Committee Member

May 2022

Acknowledgments

This thesis would not have been possible without my supervisors, and I want to start by acknowledge and thank them for the opportunity to work on this project with them. I would like to thank professor Patricia for her guidance and teaching. Working with such a strong feminine presence in science (and in life in general) has been very inspiring to me. I want to thank Marco for everything he taught me. For clarifying all my doubts, even when that meant finding out the answer himself. For reviewing this thesis (twice). For the advice, for the availability, for the dedication, for the patience and for absolutely everything else.

I would like to thank everyone at the BERM-SIXS-SPM work group. To Beatriz and Arlindo for the support and availability. To Rami and Philipp and the SIXS team for the sharing of expertise and for providing the SIXS data that was featured in this work. I have learned a lot from all the fruitful discussions I had the opportunity to follow and participate in in our meetings.

Given that I wouldn't have reached this point without concluding the other 4.5 years of university, I have to thank Miguel, Rodrigo, and Igor for being my partners in crime. They were a huge source of motivation and good mood even in hard times, and I'm not sure what my path would have been without their companionship and friendship.

I thank my grandparents, my uncles, my cousins, my brother, my boyfriend, my Inês, my Rita and the rest of my friends for always monitoring the development of this work, for hearing my complains, for celebrating my results with me, and for providing me with distractions when I needed them.

Finally, I want to thank my parents. They are approximately 99% responsible for absolutely everything that I am and for everything good that I achieve throughout my life.

Abstract

BepiColombo is the first European mission to the Hermean system. It was launched in 2018 and is predicted to enter Mercury's orbit in late 2025. It is composed of two spacecraft, ESA's Mercury Planetary Orbiter (MPO) and JAXA's Mercury Magnetospheric Orbiter (nicknamed Mio).

Among the instrument suit of the MPO is the BepiColombo Radiation Monitor (BERM), that can detect high energy protons ($\sim$1 to 200 MeV), electrons ($\sim$1 to 10 MeV) and heavy ions. BERM is part of the spacecraft housekeeping, with the objective of monitoring radiation hazards to prevent possible damage on the spacecraft and instruments. Despite not being part of the scientific payload, its capability of measuring such high energies and its operational state during all phases of the mission makes it an asset for scientific objectives as well. BERM consists of a single stack with 11 Silicon detectors interleaved by aluminum and tantalum absorbers. BERM identifies particles type and energies through the signals resultant from its interaction with the stack, assigning each particle to one of 18 channels: five dedicated to electrons, eight to protons, and five to heavy ions. The monitor provides daily files with the number of registered counts in each channel integrated over 30 seconds sampling intervals. Obtaining particle fluxes from the BERM channel counts is not straightforward. In this work, the bow-tie method, introduced by Van Allen in 1979, was applied to convert flight count rates to proton and electron fluxes. The results were used to analyse solar events detected by BERM.

Keywords

BepiColombo; BERM, Protons; Electrons; Solar Events.

Resumo

A BepiColombo é a primeira missão europeia ao sistema Hermeano. Foi lançada em 2018 e está prevista entrar na órbita de Mercúrio no final de 2025. É composta por duas naves: a Mercury Planetary Orbiter (MPO) da ESA e o Mercury Magnetospheric Orbiter da JAXA (apelidado de Mio).

A bordo da MPO está o Monitor de Radiação da BepiColombo (BERM), que consegue detectar protões ($\sim$1 to 200 MeV), electrões ($\sim$1 to 10 MeV) e iões pesados de altas energias. O BERM faz parte da manutenção da missão, com o objetivo de monitorizar os níveis de radiação para que se possam antecipar e estudar danos na nave e nos seus instrumentos. Apesar de não fazer parte do conjunto de instrumentos científicos, o facto de medir energias tão altas e o de estar operacional durante todas as fases da missão tornam-no também uma mais valia para objetivos científicos. O BERM consiste num telescópio de 11 detectores de silício, intercalados por absorvedores de alumínio e tântalo. O BERM identifica o tipo e a energia de uma partícula incidente através dos sinais elétricos resultantes da sua interação com os detetores, e atribui-a a um dos 18 canais: cinco dedicada a eletrões, oito a protões e cinco a iões pesados. O monitor fornece ficheiros diários com o número de contagens registradas em cada canal, integradas em intervalos de amostragem de 30 segundos. Obter fluxos de partículas a partir das contagens nos canais do BERM não pode ser feito de forma deterministica. Neste trabalho aplicou-se o método de bow-tie, introduzido por Van Allen em 1979, para obter os fluxos reais de protões e electrões. Os resultados foram aplicados para analisar eventos solares detetados pelo BERM.

Palavras Chave

BepiColombo; BERM; Protões; Electrões; Eventos Solares.

Contents

List of Figures

List of Tables

Acronyms

ASIC Application Specific Integrated Circuit

BERM BepiColombo Radiation Monitor

ESA European Space Agency

FITS Flexible Image Transport System

FOV Field of View

FPGA Field-Programmable Gate Array

GCR Galactic Cosmic Rays

LUT Look Up Table

MPO Mercury Planetary Orbiter

RMSE Root Mean Squared Error

SEP Solar Energetic Particle

SIXS Solar Intensity X-Ray and Particle Spectrometer

SIXS-P Particle detector of SIXS

1

Introduction

Contents

In order for a mission to be successful, any spacecraft supporting it must be able to, among other things, resist though interactions with the space environment radiation. The various possible effects of radiation, such as material deterioration, upsets in electrical compounds, component malfunction or even component loss, must be assessed thoroughly during the design of a mission's spacecraft. It is also imperative that these effects are carefully monitored during mission operation, which can be done, in part, by monitoring the radiation environment.

On the European Space Agency (ESA) led mission to Mercury - BepiColombo - this monitoring task is accomplished by the BepiColombo Radiation Monitor (BERM) [5], which was developed by the European Space Agency in cooperation with the Portuguese company EFACEC [6]. BERM is capable of operating in high fluxes of electrons with energies from $\sim$100 keV to $\sim$10 MeV, protons with energies from 1 MeV to $\sim$200 MeV, and heavy ions with a Linear Energy Transfer from 1 to 50 MeV/mg/cm^2. Even though BERM is a housekeeping instrument, it will also provide valuable scientific information about the radiation environment.

1.1 Bepicolombo Mission

BepiColombo [7] is the first ESA mission to the Hermean environment. The mission comprises two scientific spacecrafts launched together: the ESA-led Mercury Planetary Orbiter (MPO) [8], that has the main goal of studying the planet's surface and internal composition, and the JAXA-led Mercury Magnetosphere Orbiter (MMO, aka Mio) [9], that will focus on investigating its magnetosphere. Since many phenomena in the Hermean environment are highly dynamic, with both temporal and spatial variations, scientific investigations will benefit from having two spacecraft with complementary orbits and comprehensive scientific payload.

BepiColombo is set out to make a complete map of Mercury at different wavelengths and chart the planet's composition. It will also determine whether the interior of the planet is molten, investigate the extent and origin of Mercury's magnetic field, establish how big is the coupling of the interplanetary magnetic field and the solar wind with the planetary magnetosphere, among several other investigations. [4]

The mission was launched on October 20$^{\text{th}}$ 2018 and is on a seven year journey to Mercury 1.1. Its trajectory employs a solar electric propulsion system, that allows for a combination of low-thrust arcs and flybys at Earth, Venus and Mercury that are necessary to enter into orbit with Mercury with a low relative velocity. This propulsion is provided by the Mercury Transfer Module (MTM), which will separate from the two orbiters after arriving at Mercury. The calendar of the mission is shown in table.

Date	Event
20 0ctober 2018	Launch
10 April 2020	Earth flyby
15 October 2020	First Venus flyby
10 August 2021	Second Venus flyby
1 October 2021	First Mercury flyby
23 June 2022	Second Mercury flyby
20 June 2023	Third Mercury flyby
5 September 2024	Fourth Mercury flyby
2 December 2024	Fifth Mercury flyby
9 January 2025	Sixth Mercury flyby
5 December 2025	Mercury orbit insertion
14 March 2026	MPO in final science orbit
1 May 2027	End of nominal mission
1 May 2028	End of extended mission

Table 1.1: BepiColombo Mission Schedule.

1.1.1 BERM in the BepiColombo Mission

The MPO-BERM radiation monitor is part of the instrument payload of the MPO, that comprises cameras, spectrometers, radiometers, particle analysers, among others. While the 11 instruments that constitute MPO's scientific instrument suite will only be turned on during certain strategic occasions, BERM will be in operation throughout all phases of the mission and is responsible for monitoring the radiation environment. While at Mercury, and despite being a radiation monitor, BERM join coordinated observations with other instruments, with the scientific goals of studying certain phenomena, such as [4]:

- Induction effect after major solar event;
- Solar Energetic Particle (SEP) propagation inside Mercury's magnetosphere;
- SEP propagation towards Mercury's surface;
- Exosphere vs. plasma precipitation;
- Exosphere during FTE vs. external conditions;

Since BERM operates continuously during the cruise phase, other scientific opportunities will be sought during the cruise phase.

The Earth's flyby allowed to measure particle fluxes in the Earth radiation belts and particle background. This represented a particularly good opportunity to calibrate and validate BERM response functions and even to cross-calibrate its data with other instruments, including the Solar Intensity X-Ray and Particle Spectrometer (SIXS) [10]. The Particle detector of SIXS (SIXS-P) is an instrument also on board of MPO, that measures electrons and protons within an energy range overlapping with BERM's - in table 1.2 it is possible to find the energy ranges that both instruments were designed to detect.

BERM is mounted behind the radiator panel of MPO ($-$Y axis). During the interplanetary cruise phase, apart from small variations, the +Y axis of the spacecraft (figure 1.1) will be directed towards the Sun. This phase will last from 2018 to 2025 and the solar cycle will be in its ascending phase with predicted solar maximum predicted in July 2025. This will provide the opportunity to study interplanetary physics under different conditions of solar activity. The active instrument operations and BERM, in particular, will participate in solar observations, with special regard to the study of transient events such as Solar Energetic Particles, and also in the monitoring of the local radiation background due to bombardment by energetic particles of Galactic Cosmic Rays.

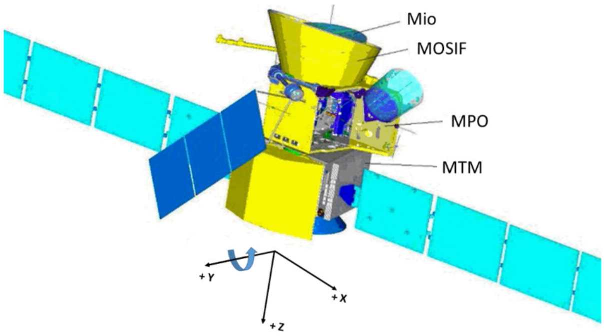

Figure 1.1: The composite spacecraft during cruise and its reference frame XYZ. From [1].

Instrument	Electron Energy Range	Proton Energy Range	Heavy Ions
BERM	~0.1 - 10 MeV	1 - 200 MeV	1-50 MeVmg$^{-1}cm^{-2}$
SIXS-P	~0.1 - 3 MeV	1 - 30 MeV	-

Table 1.2: BERM and SIXS-P detection energy range, from [4]

1.2 Thesis Outline

The main objective of this thesis is to characterize BERM performance and to analyse BERM data acquired during Solar Energetic Particle events. For this purpose, the particle event reconstruction algorithm employed by BERM was revisited and implemented in C++ to improve BERM response function computed with the Monte Carlo particle transport toolkit, Geant4. A bow-tie method was then applied, using the recomputed response functions, in order to convert the count rates measured by BERM to particle fluxes. The results were used to analyse solar events using BERM data for the first time, and to intercompare these results with the SIXS detector data, also aboard the MPO.

Chapter 2 introduces the particle environment that BepiColombo will encounter in all phases of the mission while chapter 3 provides the technical description of BERM. Chapter 4 is dedicated to study the response of BERM to electrons and protons. It describes the Geant4 simulations, developed at LIP [11], performed to characterize the instrument and ultimately, compute the response functions used in the bow-tie method. Chapter 5 describes the results of the bow-tie method that was developed. It also shows the analysis of a selection of solar events detected by BERM. Chapter 6 presents the conclusions and discusses the future work for the BepiColombo Radiation Monitor.

2

Radiation Environment in Interplanetary Space and at Mercury

Contents

Mercury is the innermost planet in the Solar System and has an unique space environment. The planet possesses a weak global magnetic field, detected by Mariner 10 [12], which is the subject of great curiosity due the small size of the planet and the fact that neither Venus, Mars or the Moon have one. This intrinsic magnetic field supports a small and dynamic magnetosphere, that is hardly able to protect the planet from the Sun's action. Table 2.1 presents a comparison between some of Earth's and Mercury's main characteristics.

Parameter	Earth	Mercury
Sun Distance (AU)	1	$0.31 - 0.47$
Sidereal orbital period (Earth's day)	365.26	87.97
Rotation Period (Earth's day)	1	58.6
Radius (km)	6371	2440
Mass (10^{24} kg)	5.97	0.33
Density (gcm^{-3})	5.5	5.4
Magnetic Field moment	31000 nT R_E^3	195 nT R_M^3
Inclination of magnetic axis to rotation axis (°)	11	0

Table 2.1: Mercury's and Earth's characteristics. Adapted from [4]

Due to its proximity to the Sun, Mercury is subject to strong solar external weather conditions, namely dense solar wind (section 2.1.1) and intense solar energetic particle fluxes (section 2.1.2). Other relevant elements of the particle environment are the Galactic Cosmic Rays (section 2.2) and energetic electron bursts in Mercury's magnetosphere (2.3.1), an intriguing form of trapped radiation (section 2.3) [13].

2.1 Solar Particles

2.1.1 Solar Wind

Solar wind is a continuous stream of electrons, ions, alpha particles and a trace of heavier nuclei, from the upper atmosphere of the Sun - the Corona [14]. Solar wind is cooled, rarefied and accelerated as it moves further from the sun, reaching supersonic speeds before reaching Mercury. It can reach velocities raging from 300 to 1200 km/s, most commonly around 400 km/s, and this speed does not change significantly with radial distance from the Sun [15]. Relevant characteristics concerning solar wind are summarized in table 2.2.

Parameter	Earth	Mercury
Solar wind speed (km/s)	320-710	250-650
Solar wind density (cm^3)	3.2-20	15-105
Proton Temperature (10^4K)	8	13-17
Interplanetary Magnetic Field (nT)	~6	31 ± 11

Table 2.2: Solar wind parameters at Mercury's and Earth's orbit. Adapted from [4]

One of the most intriguing issues concerning Mercury's space environment has been the nature of the interaction between the solar wind and the magnetosphere. For example, it is believed that such interactions are in the origin of intense energetic electron flux enhancements in Mercury's magnetosphere [16].

2.1.2 Solar Energetic Particles

Solar energetic particles (SEPs) events consist of transient high fluxes of high energy particles - protons, electrons and heavier nuclei up to Iron (Z=26) [17] - accelerated to energies in the keV-GeV range. These particles can be can be detected near planets and in interplanetary medium. These particles can be accelerated by solar flares, by interplanetary shocks driven by Coronal Mass Ejections (CME) or by shocks associated with co-rotating interactive regions [18]. Currently, the mechanisms of SEP creation, acceleration and propagation are still poorly understood, due to the inherent complexity of its three-dimensional nature, the lack of widely spread in situ observations and the complex nature of the physical processes involved. These events are destructive in nature. An event like the Carrington event [19] - the most intense geomagnetic storm in recorded history, which caused sparking and fires in several telegraph stations - could severely impact the modern technological society. It is therefore crucial to characterize and study these events.

SEP events are detected as the particle flux increases from a background level to several orders of magnitude above it, which can last from a few hours up to several days. Their consequences are a particular concern in space missions: they pose a health risk to humans and a serious radiation hazard for spacecraft. Protons are the predominant ion species measured in large events and the primary radiation hazard.

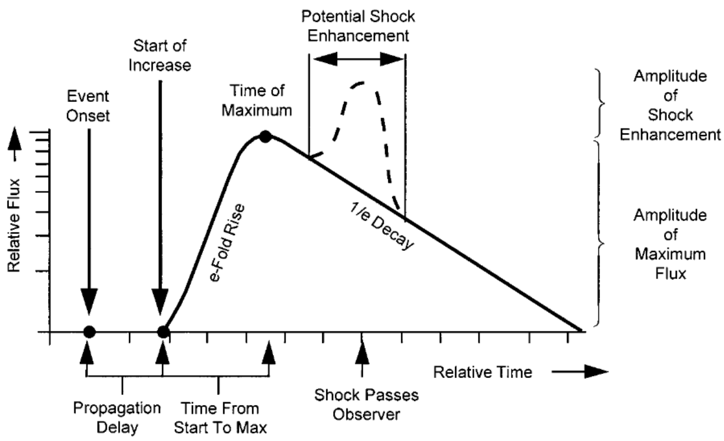

Figure 2.1: Idealized profile of a proton event. Strategic Program Plan for Space Radiation Health Research: NASA, Office of Life and Microgravity Sciences, Oct. 1998.

SEP events are usually roughly classified into two major groups: impulse and gradual. The two types differ systematically in the observed intensity profiles, the elemental abundance compositions, and the time scales of the associated soft X-ray events [18]. Impulsive events show short-duration soft X-ray emission and are associated with flare acceleration processes. They are characterized by small interplanetary ion intensities and a high electron to proton intensity ratio. Gradual events show long-duration soft X-ray emission and are associated with interplanetary shocks, driven by CMEs. They are characterized by large interplanetary ion intensities, small electron to proton ratios. The time profile of the particle flux of a gradual proton event has the idealized form of figure 2.1

2.2 Galactic Cosmic Rays

Galactic Cosmic Rays (GCR) are a homogeneous, nearly isotropic, low background of highly energetic particles, arriving from outside the Solar System with energies up to 10^{21}eV [4]. Although GCRs consists mostly of protons (~90%), there are also heavier nuclei, predominantly Helium, all the way up Uranium (Z=92). GCR's constitutes an important component of the particle radiation environment at Mercury. They continuously bombard Mercury's surface which results in cascades of secondary particles, including neutrons and gamma rays, that allow to study the composition of Mercury's surface [4]. A more accurate evaluation of the GCR flux at Mercury's orbit is required, to characterise the Hermean radiation environment and better understand this phenomenon. This, so far, has only been possible through modelling of GCR propagation in the heliosphere, with no support from in-situ observations [20].

GCR flux are inversely correlated with solar activity. During periods of low solar activity, the cosmic ray flux increases as a result of the lower magnetic cutoff exerted in charged particles as the strength of the Sun's magnetic field decreases. During high solar activity the cosmic ray flux decreases. Between a solar maximum and minimum, the GCRs flux can vary by more than one order of magnitude, depending on the particle type and energy: the lower the rigidity of the particles (the ratio between momentum and charge $|\vec{p}|/q$) the higher the flux variability. BepiColombo will measure the GCR in different stages of the Solar Cycle and at different from the Sun (0.3 to 1 AU) represents an opportunity to monitor the GCR radiation environment and to test these propagation models.

2.3 Trapped Radiation

Currently, in the solar system, Mercury Earth, all of the gas giants as well as Ganymedes (one of Jupiter's moons) possess a magnetic field and therefore a magnetosphere. The magnetosphere is the area around the planet where the magnetic field is able to exert influence on charged particles. When present, it protects it from most space radiation coming in its direction by deflecting it. At the same time, the presence of a magnetic field also gives rise to the formation of trapped particle populations,

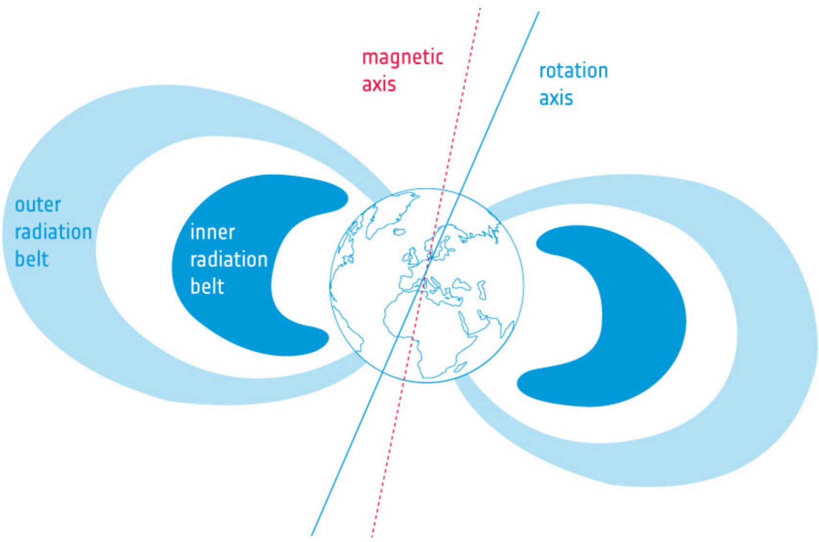

Figure 2.2: Drawing of the two radiation belts around Earth: the inner belt dominated by protons and the outer one by electrons in relation to Earth's axis. Image Credit: ESA

composed of charged particles that were not deflected, but instead trapped along the magnetic field lines. Currently, Earth, Jupiter, Saturn, Uranus, and Neptune are surrounded by trapped radiation in the form of toroidal planetary radiation belts.

Earth is surrounded by two belts: the Van Allen belts as illustrated in figure 2.2. The inner belt extends from 1 to 3 Earth radius measured in equatorial plane and consists mainly of a stable trapped proton population, with energies exceeding 100 MeV, but also of heavy ions and electrons [21]. The outer belt is dominated by electrons with energies up to 10 MeV. It starts right after a small depletion region around the inner belt, characterized by the absence of trapped particles (the slot region), and extends up to 7 – 8 Earth radius.

Mercury's magnetosphere is not strong enough to form such belts however, one of Mariner 10 most surprising discoveries, later supported by MESSENGER [16], was the detection of an abundant presence of quasi-trapped energetic electrons in its magnetosphere. It is expected that these electron bursts are related with magnetospheric activity and with solar activity, but the exact connection has yet to be established.

2.3.1 Mercury: Electron Bursts

Mariner 10 mission identified, while flying by Mercury, the presence of energetic particles in its miniature magnetosphere [22] and Armstrong et al. asserted that the signals in the proton and high-energy electron channels resulted from pileup of low energy electrons [13], instead of the reported nominal protons or high-energy electrons. During MESSENGER flybys, these magnetospheric electrons were registered as bursts lasting from seconds to hours with typical energies of 35-100 keV, with measurements of over 200 keV happening occasionally. However, no ions with energies $>$35 keV were detected anywhere in Mercury's magnetosphere, and no evidence of a stable trapped high-energy charged particle population was found. The spatial distribution of such events can be found in figure 2.3.

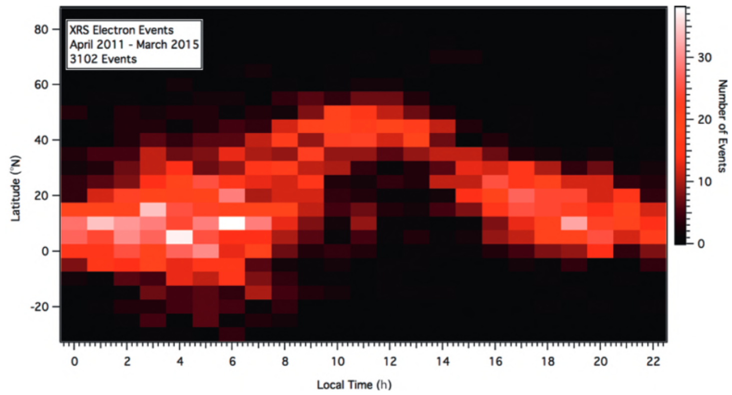

Figure 2.3: Spatial distribution of frequency of detection of supra-thermal electron events detected by the MESSENGER X-Ray Spectrometer (XRS). From [2].

These bursts were found to be related with large amplitude magnetic field changes, interpreted as terrestrial-type substorms [23] that MESSENGER data has confirmed to exist. Slavin et al. suggests that these electrons are most likely associated with an inductive electric field resulting from the rapid reconfiguration of the magnetic field at reconnecting X-lines like what happens at Earth [2]. Because of the small size of the Hermean magnetosphere, these supposed substorm-injected electrons are often unable to complete a full orbit around the planet in the azimuthal direction before being lost. This means that, in contrast to all other planets with an internal magnetic field, no "Van Allen"-like radiation belts are formed.

3

The BepiColombo Radiation Monitor

Contents

3.1 Technical Overview

The BepiColombo Radiation Monitor (BERM), present in figure 3.1a, weights 2.2kg and has a volume of 174.8L $\times$ 120.0W $\times$ 106.0H mm^3. The spectrometer is composed of a single stack of 11 solid state detectors (Silicon). Its structure is represented in figure 3.1b. The detectors have increasingly larger areas from the top detector (0.5 mm^3) to the bottom detector (900m^3). All detectors are 300 μm thick with the exception of the top one which is 200 μm thick. The detectors are interleaved by layers of absorbing material (aluminium or tantalum) with increasing thickness (0.5 to 1.5 mm). This configuration defines a Field of View (FOV) of $40°$ and was designed in order to establish the energy cutt-offs present in table 1.2. This stack of detectors is surrounded by tantalum shielding with the objective of stopping particles that come from the side or the bottom of the stack. There a collimator, which consists of a complex structure of tantalum, with a 0.5mm^2 aperture that allows BERM to operate in high particles fluxes and a 25 μm thick Beryllium window on top of the stack to cut off electrons and protons withe energies lower than ~1 MeV.

(a) Outside view.

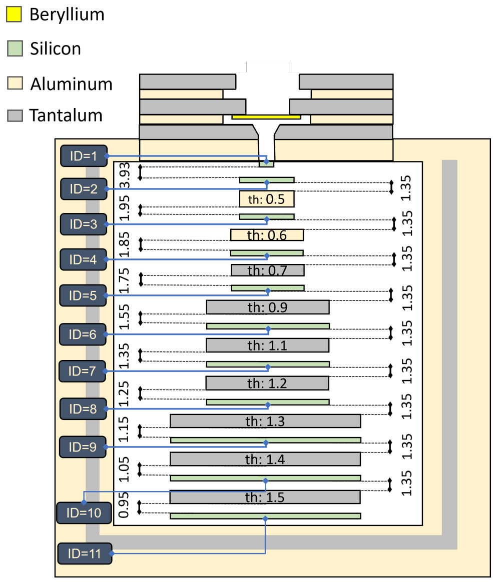

(b) Representation of inside view. Adapted from [5].

Figure 3.1: BepiColombo Radiation Monitor.

3.2 Working Principle

When a charged particle hits BERM through the telescope aperture, it will cross the different detectors and absorbing material layers, depositing energy as it travels through the stack. The energy deposition pattern (dE/dx) left in the detectors will allows to identify the type and energy (with limited resolution) of the incident particle.

3.2.1 Interaction of Particles with Matter

Charged particles moving through matter interact with the electrons of atoms in the material. The main types of interactions that lead to energy losses of the moving particle are ionization and excitation, governed by Coulomb interactions. Electrons are also often deflected by other charged particles, typically an atomic nucleus, which causes loss in kinetic energy, which in turn is converted into photons (Bremsstrahlung radiation). The cross-section of these interactions depends on the characteristics of the matter being traversed and of the incoming particle. The energy loss of energetic particles in matter is best modelled by Bethe-Bloch's formula (equation 3.1). It describes the mean energy loss per distance travelled $(-\frac{dE}{dx})$ of charged particles traversing matter, which is equivalent to describing the stopping power of the material. Figure 3.2 shows the stopping power as a function of energy for electrons, protons and heavy ions in the different materials that constitute the stack of detectors and absorbers in BERM.

$$\left\langle \frac{dE}{dx} \right\rangle = 2\pi r_e^2 m_e c^2 n_{el} \frac{z^2}{\beta^2} \left[\ln\left(\frac{2m_e c^2 \beta^2 \gamma^2 T_{up}}{I^2} \right) - \beta^2 \left(1 + \frac{T_{up}}{T_{max}} \right) - \delta - \frac{2C_e}{Z} + F \right] \tag{3.1}$$

where r_e is the classical electron radius; m_e is the electron rest mass; n_e is the electron density; I is the mean excitation of material; Z is the atomic number of material; $\beta^2 = 1 - \frac{1}{\gamma^2}$; T_{up} =min(T_{cut}, T_{max}); C_e is the shell correction function; F represent higher order corrections; z is the charge of incident particle; $\gamma = E/mc^2$; and δ is the density effect function.

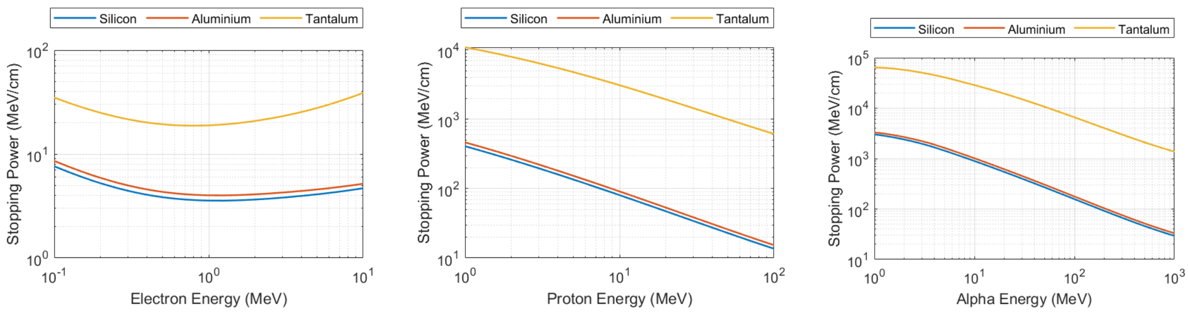

(a) Electron as the incident particle. **(b)** Proton as the incident particle. **(c)** Incident alpha particle.

Figure 3.2: Total stopping of silicon, aluminum and tantalum for electrons as function of particle energy as described by Bethe's formula. The graphs were generated using the web-based ESTAR, PSTAR and ASTAR databases provided by NIST: National Institute of Standards and Technology and the SRIM program available for download online at http://www.srim.org/

In the relevant energy range, for protons (1 to 200 MeV) and alpha particles, the incident particle energy and the deposited energy are inversely proportional - the higher the energy of the particle, the lower the rate of energy loss. For this reason protons and alpha particles will lose more energy per unit of path length just before they stop, leading to the so called Bragg peak. For electrons, this relation is not monotonous: the stopping power starts by decreasing as the particle energy increases until approximately 1 MeV, and then it starts increasing with increasing particle energy. However, the increase in stopping power is not significant and is due to Bremmstrahlung effect, which does not translate into deposited energy, given that photons can travel a long distance, or even exit the medium before interacting and depositing energy.

Throughout the energy spectrum the energy deposited by alpha particles (or heavy ions in general) is higher than the one deposited by protons, which in turn is greater than the one deposited by electrons, and this is the basis for the particle distinction done by BERM. There are, however, intersections of values of deposited energy between different types of particles: high energy protons and low energy electrons deposit similar amounts of energy (stopping power of ~ 10MeV) and the same happens for high energy heavy ions and lower energy protons (both exhibit stopping powers of $\sim 10 - 100$MeV). Higher energy particles are able to travel larger distances in the stack which allows to estimate the energy of the incident particle.

Each time a charged particle hits BERM from inside the FOV - which represents an "event" - it will cross the stack of silicon detectors until it deposits all of its energy or escapes. The ionized electrons resultant from the interactions in each detector will form the electrical signal correspondent to that detector and event.

3.2.2 Silicon Detectors

BERM's detectors are based on solid-state semiconductor technology, namely Passivated Implanted Planar Silicon (PIPS^{TM}) from Camberra.

While the electrons in isolated atoms have discrete energy levels, in solid state materials these levels merge to form two energy bands: the conduction band and the valence band. In semiconductors the two bands are neither overlapping (like in metals) nor separated by a large energy gap (like in insulators). They are characterized by a rather small energy gap: $E_G \sim 1$eV. Semiconductor solid-state detectors consist of a PN junction: two silicon layers together, where one is doped with a trivalent element (P layer) and the other with a petavalent element (N layer). The doping causes that the N-layer carries excess electrons and the P-layer carries excess holes (positive charge carriers).

When the two layers are put together, near the junction the surplus carriers in one layer diffuse to the other one. As space charge builds up, an electrical potential is formed, inhibiting diffusion. This potential creates a depletion region that quickly sweeps any charge created by high energy particle interaction. By applying a negative potential between the p and n sides, the depletion region is increased until the device is fully depleted. BERM operates in these regime with a potential of 50 V.

An incoming charged particle interacts with the depletion region to form electron-hole pairs. The energy necessary to form a single electron-hole pair depends on the detector material (3.6 eV on average for silicon), but is essentially independent of the energy of the incoming particle. The number of created electron-hole pairs is thus directly proportional to the energy deposited by the particle. The electric field in this region sweeps the electrons to one terminal and the holes to the other. The resultant charge pulse forms the electrical signal to be interpreted.

3.2.3 Readout

BepiColombo mission operates with limited downlink bandwith. For that reason the particle events detected by BERM are processed in flight before the information is sent to Earth. This processing consists on assigning each particle event to a particle channel based on the electrical signal (or lack of) in each detector. BERM delivers a daily file with all the number of events detected in each channel, that act as counters, summed over 30 second sampling intervals. The 20 channels consist on 5 bins for electron, 5 for heavy ions, 8 bins for protons (see table 3.1), one for vetoed events and one for unidentifiable events.

Particle	Electrons					Protons								Heavy Ions				
Channel	1	2	3	4	5	6	7	8	9	10	11	12	13	14	15	16	17	18
Low Energy Limit (Unit)	0.1	0.3	0.5	1.1	2.6	1.2	5.9	9.1	13.0	20.7	31.4	59.1	80.1	1.0	2.2	4.8	10.5	22.9
High Energy Limit (Unit)	0.3	0.5	∞	∞	∞	5.9	9.1	13.0	20.7	31.4	59.1	130	160	2.2	4.8	10.5	22.9	50.0
Unit	MeV													MeV/(mg·cm^2)				

Table 3.1: Energy range of each particle channel. Most bins are sensitive to energies higher than shown here but with lower sensitivity. The interval limits for electron and proton channels were determined in [5], the ones for heavy ions are according to BERM manufacturer information due to lack of further study.

3.2.3.A Signal Processing

The electrical signals generated by a passing particle in BERM's silicon detectors is read by a dedicated VA32TA2.2 Application Specific Integrated Circuit (ASIC), developed by IDEAS (datasheet obtained per request from www.ideas.no). The ASIC layout is depicted in figure 3.3. Each ASIC channel (connected to one of the detectors) is composed by a VA and a TA unit. Input signals in each ASIC channel are amplified and divided between their VA and TA units. The signals are processed by the TA unit which resorts to a fast-shaper, that will rapidly (75 ns) integrate the signal and trigger the reading in the VA unit of all detectors, in case the amplitude of the measured signal is above a certain threshold (V_{THR}). During flight, only the top detector is used to trigger the reading. The triggering resorts to the on-board's Field-Programmable Gate Array (FPGA), which collects the trigger signal and activates the Sample/Hold circuit so the signals can be read via an analogue multiplexer. The slow shapers in the VA units integrate the signal for up to 2 µs (programmable). The discharge time of the slow shapers is of 10 us which limits the readout to 100 kHz. The readout of the detectors' signals is then converted into a 14-bit digital signal by an analog-to-digital converter (ADC) with the zero corresponding to the maximum value, i.e a null signal in the detector would correspond to 32767 ADC.

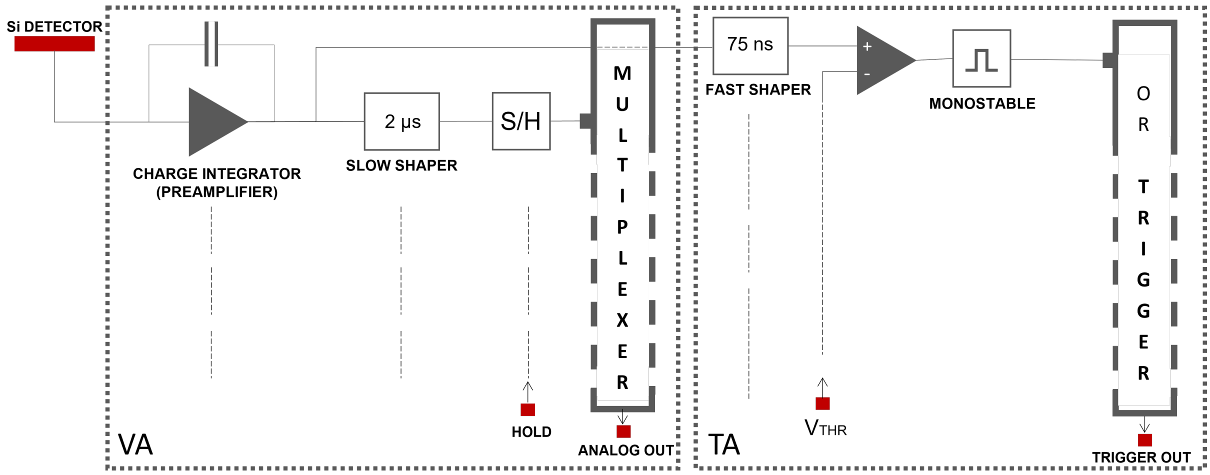

Figure 3.3: Representation of VA32TA2.2 ASIC, responsible for reading the detectors' signals in BERM.

In terms of digital processing, the first step is to invert the 14-bit signal. Due to intrinsic noise sources (e.g, associated electronics) the detectors will have a signal, even when there is no particle crossing them. This noise signal was measured for each detector (ADC_{ID}) during the calibration campaign, fully described in [5], and it is the ADC value that the electronic 0 actually corresponds to (see Pedestal in table 3.2). Therefore, after inverting the obtained signal, the pedestal must be subtracted to retrieve the signal that was actually produced by the radiation. Finally, the fact that different detectors have different areas influences the correct reading of all the signals, since this is done simultaneously. Due to their larger capacitance, the signals of the larger detectors are not read at their peak amplitude, a fact that must be accounted for and compensated by weighting the signals. After inversion and pedestal removal, the signal's amplitude in each detector will be multiplied by its weight factor ($W_{ID}^{PEDESTAL}$, which was determined in previous works) in order for them to be in equal footing for comparison: larger detectors have higher weighting factors (see table 3.2). All the values for the pedestal and weight factors are stored in BERM's Look-Up Table (LUT), and can be updated in future calibration revisions if the instrument aging requires so.

3.2.3.B Particle Identification Algorithm

To determine the incident particle type and energy, the detection algorithm starts by finding the detector (ID_{MAX}) where the largest amount of energy was deposited (ADC_{MAX}). It will then perform a VETO analysis to determine whether or not the reading corresponds to a relevant event. It is possible that the detection system is triggered by some phenomenon in the first detector other than a passing particle (e.g, noise due to crosstalk with other detectors), and if this coincides with a side hit of a particle that was able to cross the detector shielding, that particle will incorrectly be considered as an event. Therefore, a veto analysis must be performed to confirm that the signal in the first detector that triggers the detection

Detector ID	1	2	3	4	5	6	7	8	9	10	11
Radius (mm)	0.4	4		6.9		11.95			16.95		
Thickness (mm)	0.2	0.3									
Zero (ADC)	1504	1575	1598	1473	1399	1498	1606	1456	1398	1551	1543
Weight	1	1	1	1.2					1.4	1.6	1.8
Veto (ADC)	8					12			32		NA
Energy to ADC coefficient (ADC/MeV)	836.28	1098.10	1198.30	1136.20	1204.80	975.31	958.49	931.27	826.31	807.05	855.06

Table 3.2: BERM detectors specifications.

system is indeed from a particle that passed through all the detectors until ID_{MAX}. Each detector has a minimum signal amplitude - ADC_{VETO} - above which it is considered to have been originated by the passing of a particle, and under which it should be disregarded and assumed to be noise. The veto analysis consists of checking whether the signal's amplitudes in the detectors preceding ID_{MAX} is greater than their veto values validate the event if they are. If they are not, the event will be vetoed and considered as a count for channel 19.

The next step is to determine the particle's type. The FPGA compares the largest signal and the signal of the detector that precedes it (ADC_{MAX-1} and ID_{MAX-1}) with threshold values that correspond to the minimum and maximum energies that an electron, a proton, and a heavy ion can deposit in those detectors (see table 3.3). Minimum for electrons is the veto value, and there is no maximum for heavy ions. The intervals defined by these thresholds have no intersection. The particle is identified by determining to which interval – electron, proton, or heavy ion – the signals correspond to. If it isn't possible to place the signals in an interval, the event will be considered to be unidentifiable and considered as a count for channel 20. After identifying the incident particle's type, the system will assign it to a channel. In table 3.4 is possible to find which channels can be attributed depending on which detector the maximum amount of energy is deposited. This is accomplished by creating a 17-bit address containing information regarding the particle type, the detector with larger deposited energy and a selection of 11 bits of the signal measured in the detector that precedes it (see figure 3.5). This address is then searched in the LUT that will associate a bin to the event. The whole process is summarized in figure 3.4.

The ADC_{VETO} values and the threshold to determine the particle type, as well as the association between address and particle channel, are all stored in the LUT and can be updated in the future, if required, to improve the instrument's function or to account for its aging.

During BERM development, the threshold value above which the reading is triggered was left in its default value and no calibration was performed to study it. This means that at the moment it is not completely clear how much energy a particle must deposit in the first detector in order to trigger the reading. The analysis of experimental calibration data, performed at the PSI - Paul Scherrer Institute, resulted in finding the ADC-to-Energy coefficients to convert the digital signal in the detectors - in ADC - into energy units and vice-versa (see table 3.2). These data also allowed to estimate the threshold value to be $ADC_{\text{th}} = 180 \pm 20$ or $E_{\text{th}} = (220 \pm 20)$ keV. [5]

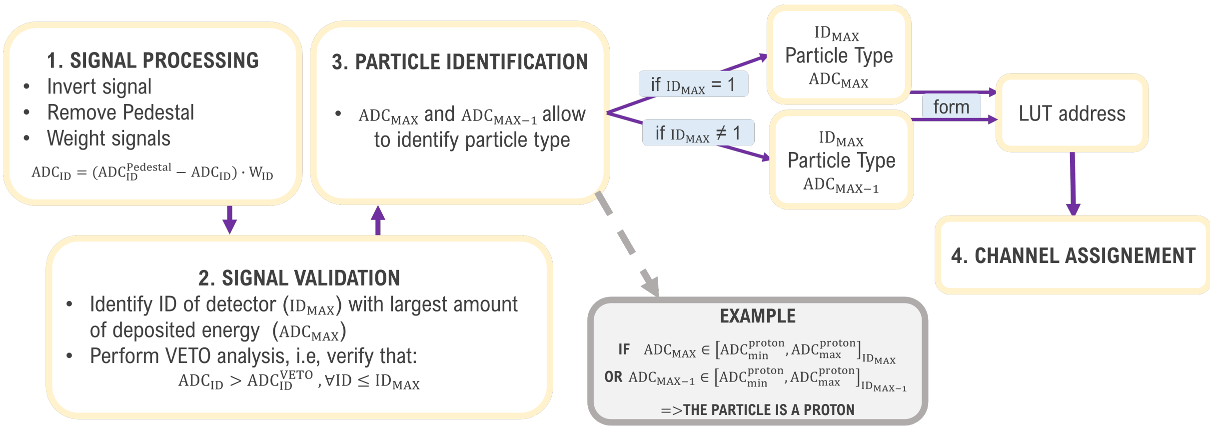

Figure 3.4: Representation of signal processing (step 1) and particle identification algorithm (steps 2-4) of a detected event.

Detector	1		2-11	
Unit	ADC	MeV	ADC	MeV
$ADC_{max}^{electrons}$	299	0.36	299	0.24 - 0.37
$ADC_{min}^{protons}$	300	0.36	300	0.25 - 0.37
$ADC_{max}^{protons}$	5999	7.17	5999	4.98 - 7.43
$ADC_{min}^{heavy\ ions}$	6000	7.17	6000	4.98 - 7.43

Table 3.3: Threshold values that correspond to the minimum and maximum energies that an electron, a proton, and a heavy ion can deposit in those detectors. The threshold in MeV for detectors 2-11 pose as range of values due to the different detectors having different ADC-to-Energy coefficients.

ID_{MAX}	Channel																	
	1	2	3	4	5	6	7	8	9	10	11	12	13	14	15	16	17	18
1	X	X				X								X				
2			X				X	X						X				
3			X						X						X			
4				X						X					X			
5				X							X					X		
6					X						X					X		
7					X							X					X	
8					X							X					X	
9													X					X
10													X					X
11													X					X

Table 3.4: Channels that can be attributed to an event depending on the detector in with the maximum deposited energy.

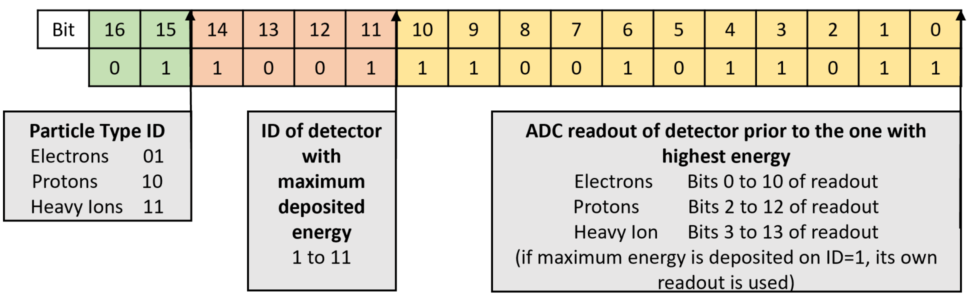

Figure 3.5: Energy reconstruction LUT address schematic.

4

BERM Response to Protons and Electrons

Contents

4.1 Methods: BERM Simulations

To use and interpret BERM data, it is critical to precisely characterize its behaviour. For this purpose, it is necessary to study how energetic particles interact with it. The interaction of charged particles with BERM is too complex to be described by a solvable mathematical expression or even to be treated in a closed, deterministic way. Some of the underlying physical processes involved are themselves inherently non-deterministic. Because it is not possible to reproduce the space environment on the ground, computational simulations are necessary to describe these interactions. If a sufficient number of particles is simulates, a statistically reliable description of the interactions can be obtained.

4.1.1 Geant4 Simulation

Geant4 (GEometry ANd Tracking) is a widely used toolkit for the simulation of the passage of particles through matter resorting to Monte Carlo methods. It includes methods to describe geometry, tracking, physical interactions, detector response, run management, visualization and user interface. [24]

To characterize BERM, an in-house Geant4 application was developed at LIP. [5]. The application allows to simulate a set of primary particles that are tracked as they interact with a computational model of BERM. These interactions are calculated step by step until the particles have deposited all of their energy or until they leave the geometrical model, resorting to well-established interaction cross sections for the physical processes involved, as implemented in the Geant4 toolkit. [24]

BERM was integrated in this simulation (as represented in figure 4.1) by converting its detailed mechanical description in a STEP (Standard for The Exchange of Product Data) file to Geometry Description Markup Language (GDML), via GUIMesh [25]. The particle source consists of a rectangular planar source with a 120×123 mm^2 area. The spatial distribution of the particles was considered to be isotropic, and its energy spectrum was assumed to follow an inverse power law, normalized to a flat energy spectrum in order to optimize the computation time. [5]

The outputs of these simulations are analysed by a first C++ code, via ROOT, that mimics BERM algorithm (described in section 3.2.3.B and summarized in figure 3.4). The output of this code is a set of ROOT files, that stores all relevant information by agglomerating it in several histograms that allow to analyse different physical properties. Some examples include the influence of initial energy on energy deposition in each detector, the influence of initial particle position on channel attribution, among many others. To study the behaviour of incident protons and electrons in the monitor, a total of 8 files were created, each corresponding to a particle type and a certain energy range, as displayed in table 4.1.

In order to mimic BERM's algorithm, this C++ code takes as input, besides the results of the Geant4 simulations, the Look Up Table (LUT) where all the relevant parameters for the particle identification algorithm are stored, as well as the electronic threshold that triggers the detection system. The LUT

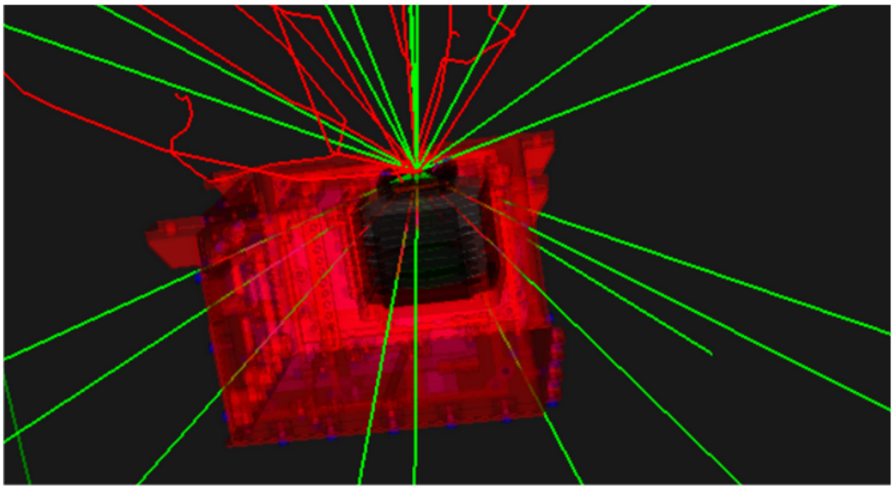

Figure 4.1: Representation of the Bepicolombo Radiation Monitor as implemented in Geant4 simulations.

Files	Particles	Energy (Mev)	Number of simulated particles
E1PF.root	Electrons	0.1 - 2.0	18$\times 10^9$
E2PF.root	Electrons	2 - 10	5$\times 10^9$
P1PF.root	Protons	0.1 - 2.0	7$\times 10^9$
P2PF.root	Protons	2 - 10	10$\times 10^9$
P3PF.root	Protons	10 - 80	10$\times 10^9$
P4PF.root	Protons	80 - 150	1$\times 10^9$
P5PF.root	Protons	150 - 250	1$\times 10^9$
P6PF.root	Protons	250 - 1000	81$\times 10^6$

Table 4.1: List of output files from Geant4 simulation analysis. Each file contains a total of histograms that agglomerate relevant information concerning the interaction of the spectrometer with the particles corresponding to that file.

that is used as input is a copy of the one used in the flight model. The values in it can be changed to study possible improvements in the flight unit. Even though it is programmable in the ASIC and no in the LUT, the same is true for the detection trigger threshold. In this analysis, the value obtained from the calibration analysis (220$\pm$24 keV) was used but it can be tuned in the future.

4.1.2 Analysis of simulations' ROOT files

In terms of characterization, the main task at hand during this work was to understand the behaviour of the algorithm and of the spectrometer itself in terms of channel attribution. The developed C++ codes manipulating the relevant histograms in order to study the response of the channels, as a function of incident particle energy. An example of such histograms is in figure 4.2.

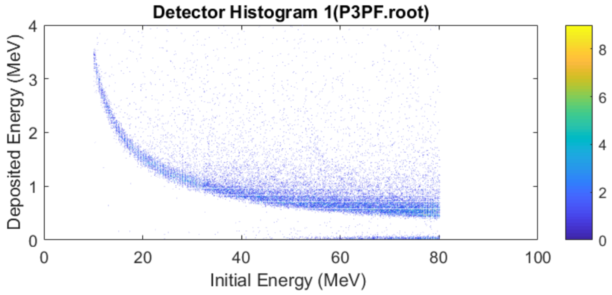

Figure 4.2: Detector 1 Histogram - For a given detector, it describes the number of times that a particle with a certain initial energy, deposited a certain amount of energy on the detector. The bins' width is 0.1 MeV for initial energy (x axis) and 0.01 MeV for deposited energy (y axis). There are 11 histograms (one per detector) of this type per ROOT file. The set of these two-dimensional histograms was used to study the patterns of energy deposition in the detectors.

4.2 Discussion: BERM Response to Protons and Electrons

As mentioned in previous sections, BERM can attribute an event to one of the 18 particle channels, out of which the first five are dedicated to electron detection, the following 8 to protons and the last 5 to heavy ions. However, due to detector design and algorithm implementation, under certain circumstances, particles type will be misinterpreted and attributed to channels outside of the ones dedicated to detect them. This means that, for each incident particle type, the response of all 18 channels should be studied to fully understand the behavior of the monitor. Table 4.2 shows the naming convention corresponding to the 18 channels, depending of the particle type. This nomenclature (P, E, EP, PE) will be used when talking about the channels as regard to their response to protons and electrons. However, their original numbering (1 to 18) will also be required when discussing characteristics of the channels that are independent of the incident particle type.

BERM Flight Channel	1	2	3	4	5	6	7	8	9	10	11	12	13	14	15	16	17	18
Incident Protons	EP1	EP2	EP3	EP4	EP5	P1	P2	P3	P4	P5	P6	P7	P8	HP1	HP2	HP3	HP4	HP5
Incdident Electrons	E1	E2	E3	E4	E5	E6	PE1	PE2	PE3	PE4	PE5	PE6	PE7	PE8	-	-	-	-

Table 4.2: Names of the channels, depending on the type of particle they are being used to measure.

In the scope of this work only incident protons and electrons are analysed. The behaviour of the detector for heavy ions will be studied in future works.

4.2.1 Response to Protons

When a proton hits BERM through the collimator aperture, it will start by interacting with the first detector. Its ability to reach the next detectors depends on the particle type and energy. As mentioned before, a low energy proton loses energy at a higher rate than a high energy one. This can be seen in figures 4.3 and 4.4, where the deposited energy in each detector is displayed as a function of proton energy. The curves in figure 4.4 correspond to mean values, obtained from the curves in figure 4.3.

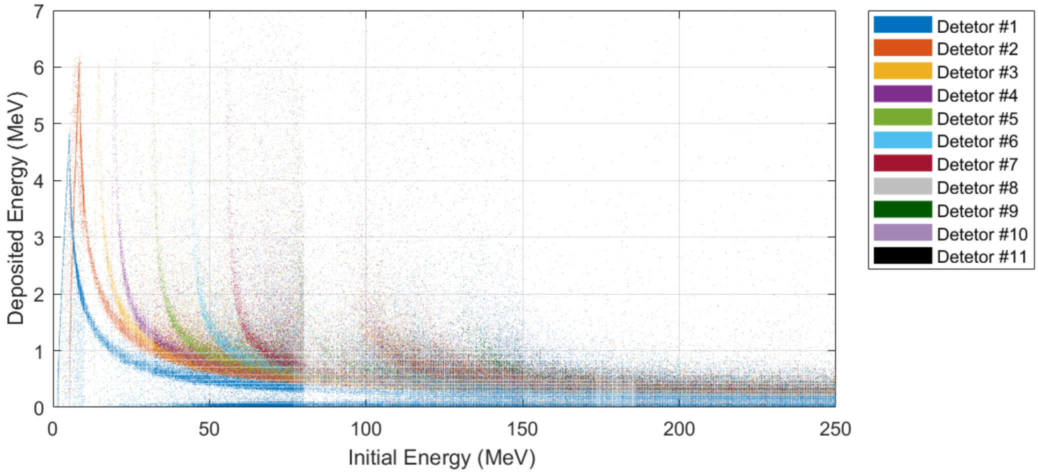

Figure 4.3: Deposited energy in each detector, as a function of the incident proton's initial energy. For each detector curve, one point corresponds to one simulated particle

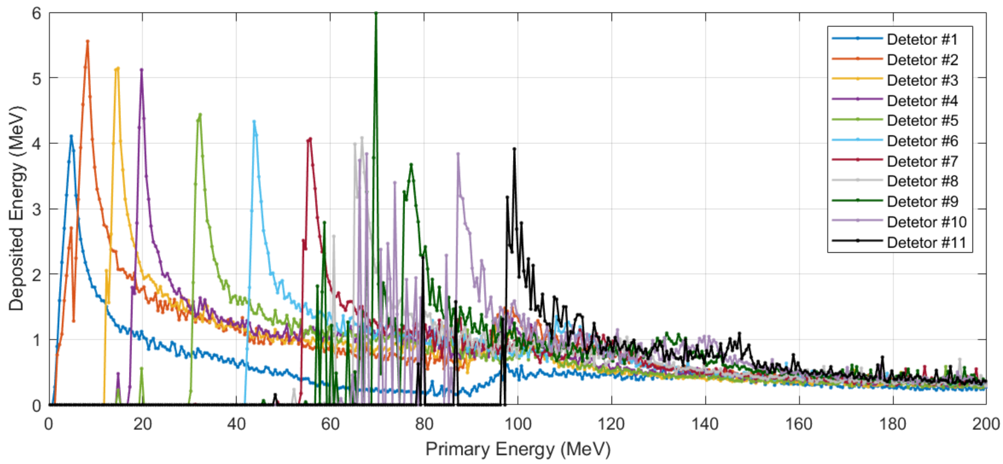

Figure 4.4: Mean energy deposition pattern as a function of initial energy of an incident proton, in each detector. It is possible to see that each curve possesses a peak for certain values of primary energy that will cause its corresponding detector to be determined as ID_{MAX}.

All curves in figure 4.4 have similar behaviour. Each curve begins at the minimum initial energy a proton must have to reach that given detector, e.g only protons with energies greater than 12 MeV are able to cross the first two detectors and reach the third one. At the beginning of the curve, particles deposit all of their kinetic energy. As the incident particle energy increases, the particles deposit less energy in the detector before exiting it. This is due to the fact that the lowest the incident energy of the proton, the greater the amount of energy it deposits. This descending tendency is actually perturbed by what seems to look like a second defaced peak, starting at a primary energy of 90 MeV in the first detector (see figure A.1 for a clearer visualization of this effect). This second peak happens due to high energy particles that are able cross the tantalum and aluminum collimator. These are particles that have lost a fraction of their energy in interactions with the collimator material, and consequently deposit more energy in the detector than expected for their initial energy value. When these particles hit the first two detectors, the signal is strong enough to trigger a reading causing bin P1 (channel 6, associated to detector #1) to be highly contaminated by high energy protons, given that this channel is associated with the largest signal on the top detector. This fact is supported by the high sensitivity of P1 to protons above 100 MeV, evident in figure 4.5). Despite coming from outside BERM's field of view ($40°$), some of these particles are able to pass the first detector and reach the second one, given that the equivalent FOV between the detectors 1 and 2 is $75°$. For that reason, and possibly also due to electronic cross talk between the two detectors even when the particles only hits crosses the second one, there is also a high sensitivity of bin P2 (channel 7, associated to detector #2) to protons with more than 100 MeV.

In figure 4.4 the regions where the deposited energy curve of a given detector stands above the rest can also be identifiable, i.e to which energies that detector will be the one with the highest amount of energy deposition (and identified by the algorithm as $\mathrm{ID_{MAX}}$). For example, a proton that has an energy of 50 MeV will produce the highest signal in detector 6 and therefore will be attributed to channel 11 (according to table 3.4), referred to as P6. The ability to perform this analysis is crucial to understand the behaviour of the algorithm, to detect possible flaws in it and know how to correct them.

The previous analysis is useful to better interpret the sensitivity of the different channels depending on the particles' initial energy, i.e the channels response functions. This can be expressed in terms of the channel's geometric factors as a function of the kinetic energy of the incident particles. The geometric factor of a channel is calculated according to equation 4.1, for a source area A and considering a hemispherically isotropic angular distribution around the surface normal to each dA of the source.

$$F_R(E) = A\frac{N_{channel}(E)}{N_{Inc}(E)}\int_0^{2\pi} d\phi \int_0^{\frac{\pi}{2}} \sin\theta\cos\theta d\theta = A\pi\frac{N_{channel}(E)}{N_{Inc}(E)} \tag{4.1}$$

where $N_{channel}(E)$ is the number of simulated particles fulfilling the criteria of being detected in the relevant channel at energy E and $N_{Inc}(E)$ is the number of total incident particles with energy E.

The BERM channels geometric factors for incident protons were determined in [5] and are reproduced below - in figures 4.5 and . The geometric factors of the 8 proton channels are represented in 4.5, whereas the geometric factors of the 5 electron and 5 heavy ion channels in response to protons are represented in figures 4.6a and 4.6b, respectively.

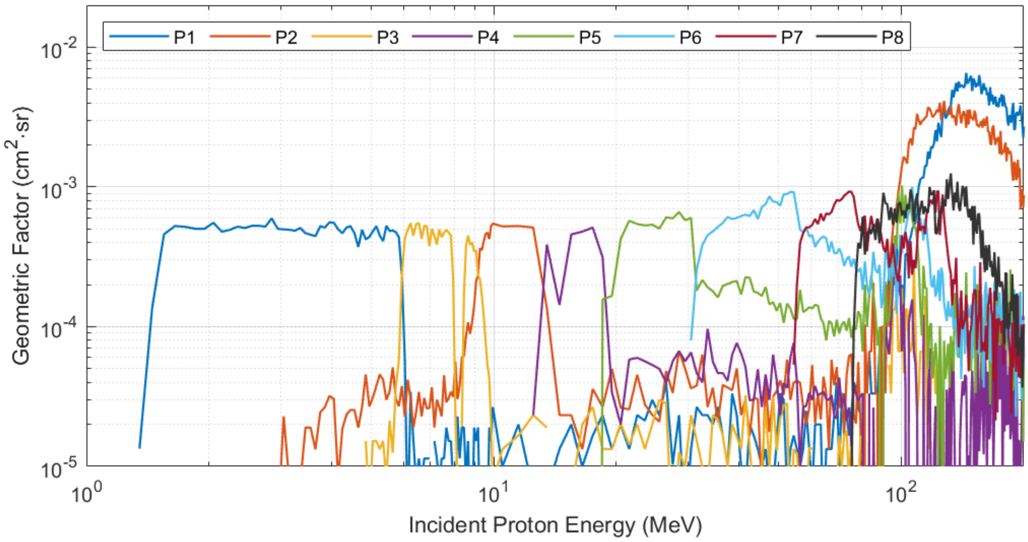

Figure 4.5: Geometric factor of the 8 proton bins (channels 6 to 14 in table 3.1) to incident protons with energies varying from 0.1 MeV to 250 MeV.

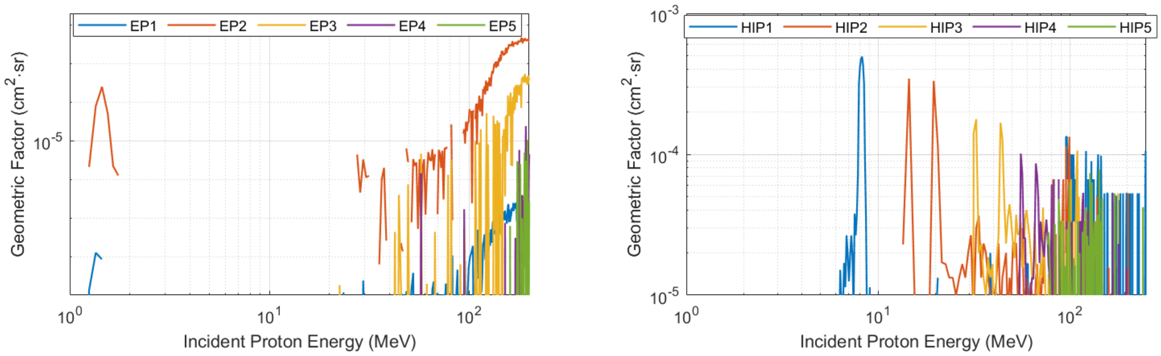

(a) Geometric factor of the 5 EP bins - channels 1 to 5 to incident protons with energies varying from 0.1 MeV to 250 MeV.

(b) Geometric factor of the HIP bins - channels 14 to 18 - to incident protons with energies from 0.1 MeV to 250 MeV.

Figure 4.6: Geometric factor of EP bins (electron channels as proton channels) on the left and HIP bins (heavy ion channels as proton channels) on the right.

The response of proton bins P1 to P5 have boxcar like shapes and were therefore considered to be differential channels. The functions of bins P6 to P8, on the other side, do show a steep increase starting from a certain threshold energy, but do not show a steep decrease, meaning that their sensitivity remains similar as energy increases, which led to them being considered as integral channels.

One thing to note in figure 4.5 is that there are non coincident regions of dominance for each channel, that are in accordance with what one would predict based on figure 4.4. However, the response functions have some intriguing features that require further discussion.

The first one is that there is an unexpected swap between bins P2 and P3 (correspondent to channels 7 and 8): particles that are attributed to bin P3 will have smaller incoming energies than the ones attributed to P2. This is explained by the behaviour of the algorithm in conjunction with the energy deposition pattern shown in figure 4.4. Detectors 3 to 11 can only assign a maximum of one bin for each particle type (see table 3.4), meaning that in these cases the 6 most significant bits of the LUT address will suffice to determine the channel of the event (see figure 3.5). However, if maximum energy is deposited in detector 2, two channels can be assigned: channel 7 and 8. This means that the 11 least significant bits of the address will also be relevant to find the channel of the event. For this detector there is an address limit under which the particle will be assigned to channel 7 and above which it will be assigned to channel 8. However, this implementation is not well suited for this detector. When maximum energy is deposited in detector 2, the LUT address will use the signal of energy deposition left in detector 1: a higher amount of deposited energy corresponds to a more intense signal and (as it is currently implemented) to a larger LUT address number. As illustrated in the scheme in figure 4.7 (a zoomed analysis of figure 4.4), when maximum energy is deposited in detector 2, the energy deposition in 1 is already in the descending part its curve. Therefore, a lower energy deposition in detector 1 corresponds to a higher incident particle energy, which is contrary to the LUT addressing. For that reason, the protons that are assigned to channel 8 are in fact less energetic than the ones assigned to channel 7, which results in the inversion of bins P2 and P3 in figure 4.5. Although this inversion does not apparently represent any technical liability in terms of data analysis, it can be corrected easily by updating the LUT: the addresses that currently corresponds to channel 7 would have to correspond to channel 8, and vice versa.

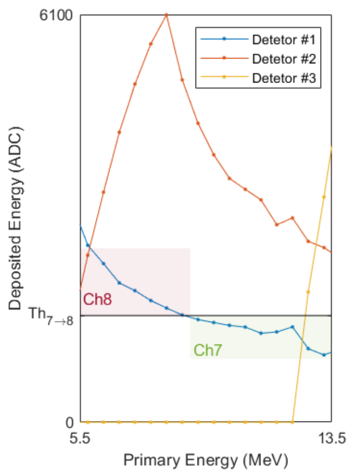

Figure 4.7: Representation of deposited energy in detector ID=1 when maximum energy is deposited in ID=2. It illustrates that the LUT addressing when is incorrectly implemented for ID_{MAX}=2 which causes the channel inversion in P1 and P2's geometric factors.

One other feature of the response functions that is noteworthy, is the high geometric factor of P1 and P2 to high energy protons. This is a physical phenomena that is hard to disentagle and that tampers data analysis for these two channels when protons with energies above 90 MeV are present.

The final feature/problem to be discussed in the response functions of proton bins 1 to 8 concerns the discontinuity in P3's response function around 8.25 MeV, that splits the function from one boxcar into two. This happens because a particle that deposits maximum energy on detector 2 can deposit up to 5.5 MeV, corresponding to 6096 ADC as depicted in figure 4.8, which is above the 6000 ADC threshold to be interpreted as an heavy ion. For that reason, the protons in that region are in fact being considered as heavy ions (in HP1), as showed in figure 4.6b.

In fact, the response functions for all heavy ion channels consist of a total of 7 distinct spikes. The energies where each of these spikes happens correspond to the incident energies where the maxima of energy deposition occur. Although in figure 4.8 the curves of detectors 4-6 do not exceed the limit of 6000 ADC, it should be noted that these are average deposited energy curves, and stochastically there will be particles that deposit energies greater than 6000 ADC (see figure 4.3, although the deposited energy is shown in MeV and not in ADC). The reason why HP2, HP3 and HP4 exhibit two spikes each is because each of these channels is associated to two detectors (see table 3.4). These spikes can therefore be incorporated into the geometric factor of the proton channels (where they belong) if the threshold to distinguish between protons and heavy ions is increased in a future update of the LUT.

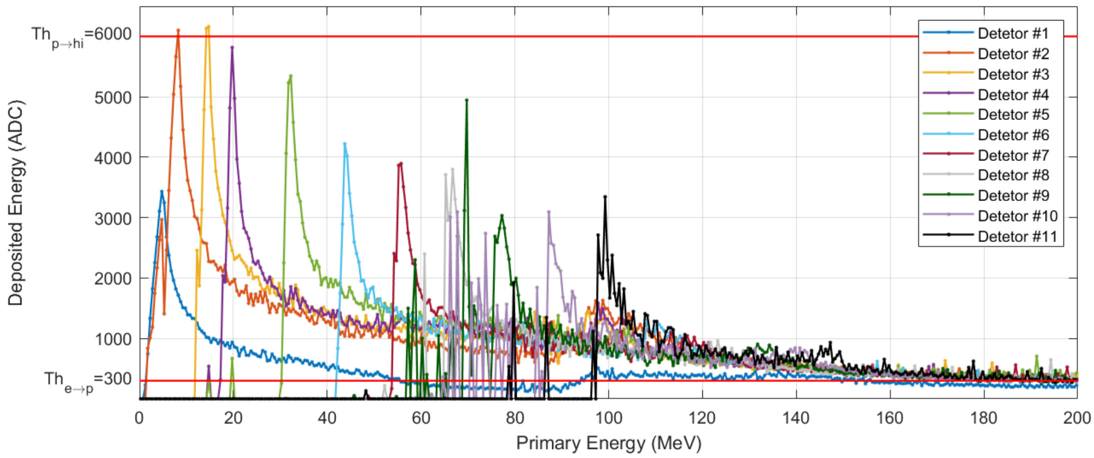

Figure 4.8: Mean deposited energy (in ADC) as a function of initial energy of an incident proton, in each detector. The thresholds used to distinguish between particles are identified by red lines to show that protons will be misinterpreted as heavy ions (for energy deposition above $\text{Th}_{p\rightarrow hi}$6000) or as electrons (for energy deposition below $\text{Th}_{e\rightarrow p}$300)

The EP channels (i.e, electron channels measuring protons), are also sensitive to highly energetic protons (>100 MeV). This is expected since highly energetic protons interact very little with matter and can be misinterpreted as electrons, when they deposit energy that is smaller than the value corresponding to 300 ADC: the threshold below which particles are classified as electrons. However there is also contamination of EP1 and EP22 with low energy protons (∼1MeV) which happens because they deposit an amount of energy in the detectors that is again lower than the 300 ADC, despite representing a large proportion of their initial energy.

4.2.2 Response to Electrons

Figure 4.9 shows the mean energy an electron deposits in each detector, according to its initial energy. In detectors 1 to 4, there a rise in the beginning of the deposited energy curve, as it happens with the protons, although this slope for electrons is not as steep. However, unlike for protons, after descending slightly the deposited energy curves in the detectors 1-4 stabilize at an approximately constant value as incident particle energy increases. The deposited energy curves in detectors 5 to 8 have low statistical significance because electrons with energies below 10 MeV seldom reach those detectors.

An important fact to acknowledge is that, according to figure 4.9, the average energy deposited by electrons in detector 1 is always below 0.220 MeV - the estimated threshold value for triggering the detection system, as discussed in section 3.2.3.B. This means that BERM might struggle in detecting low fluxes of electrons, given that most electrons are unlikely to trigger the detection system. This is particularly relevant for channel 1. According to the LUT, a particle is assigned to channel 1 when the maximum energy is deposited in the first detector and if this deposition corresponds to a signal lower than 178 ADC (or 212 keV). This value is smaller than the mean value for the trigger threshold (180$\pm$20 ADC), which means that a large portion of the events that could be attributed to channel 1 are being lost by the detection system.

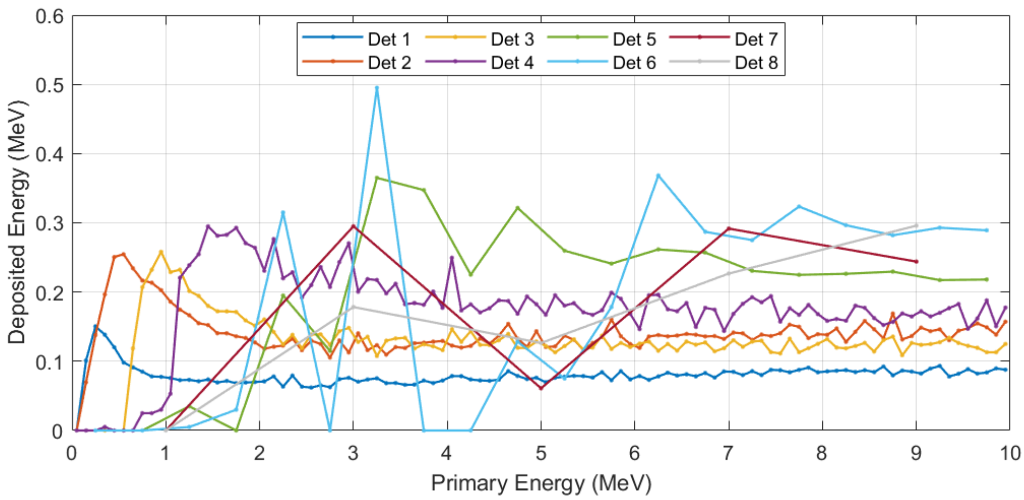

Figure 4.9: Mean deposited energy as a function of initial energy of an incident electron, in each detector. Detectors 9 to 11 do not attribute electron channels and are therefore not represented.

The deposited energy curves in detector 1 in figure 4.9 also reflect the different amplitudes of the geometric factors of the different channels in 4.10. The decreasing trend of the amplitudes of the geometric factors channels E2 to E4 is related to the decrease in probability of an electron reaching detectors located deeper in the stack. This trend is not followed by E1, that presents itself with the lowest geometric factor ($\sim 10^{-9}$ cm^2·sr) due to the high detector threshold value.

Electron channels (figure 4.10) seem close to integral form. However bins E1 and E2 display clear peaks in the beginning of their response curves making them much more sensitive to those energies than for higher energies and were therefore considered to be differential channels.

In figure 4.11 the geometric factors of PE channels are represented. Proton bins 1, 2, 4, 5 and 6 are sensitive to electrons, and therefore subjected to contamination in multi-particle environments. EP1, EP2 and EP4 are well behaved integral channels, so they can provide useful information related to electrons if the right conditions, i.e. proton-free events, arise.

Heavy ion channels do not yield any result: the energy deposited by electrons is never high enough for them to be misinterpreted as heavy ions.

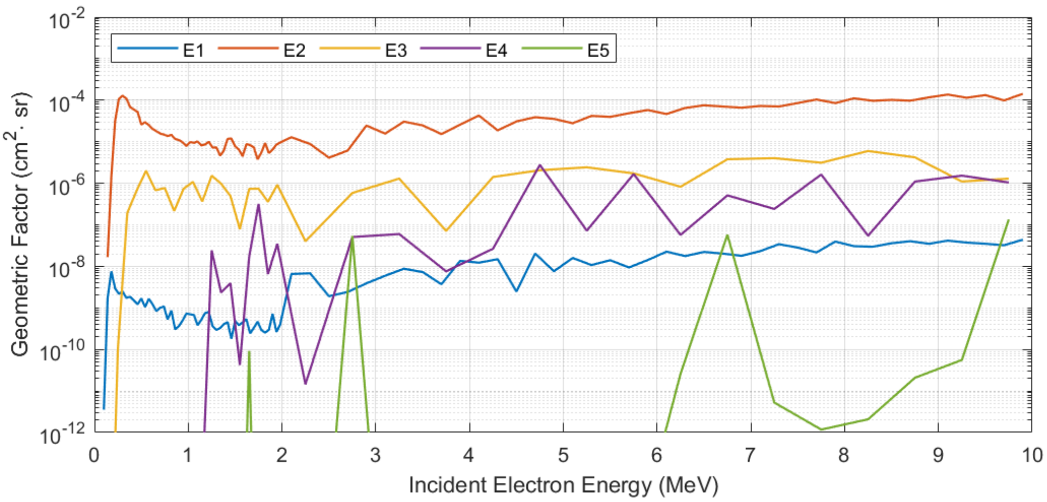

Figure 4.10: Geometric factor of the 5 proton bins (channels 1 to 5 in table 3.1) to incident electrons with energies varying from 0.1 MeV to 10 MeV.

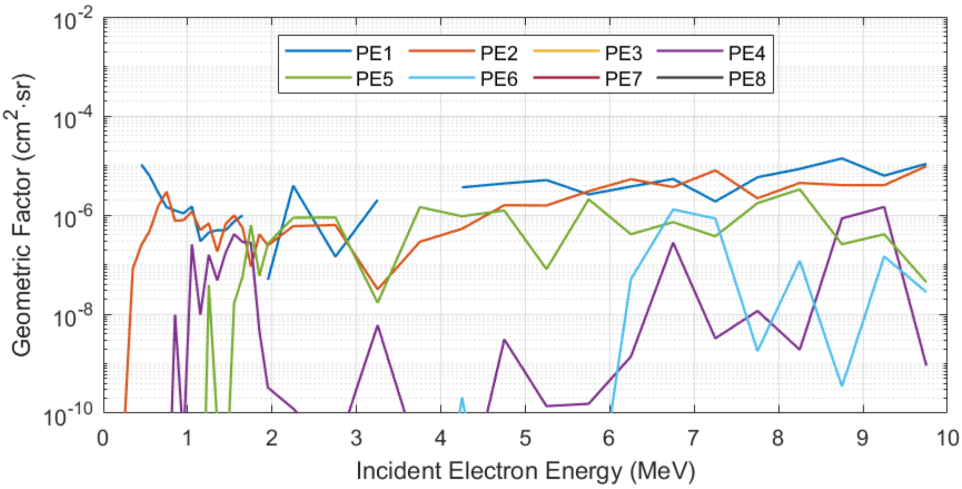

Figure 4.11: Geometric factor of the 8 PE bins. It represents how sensitive (proton) channels 6 to 13 are to incident electrons with energies varying from 0.1 MeV to 10 MeV.

5

BERM Flux Reconstruction for Flight Data Analysis

Contents

The data provided by BERM consists of raw count units for all 20 channels, reccorded in Flexible Image Transport System (FITS) format in daily files, with 30 second sampling intervals. Given the broad energy interval corresponding to each channel (see figures 4.5 and 4.10), the raw count rates have no physical meaning. For this reason, it is necessary to convert them to physical units (energy and particle flux) in order to determine the particle fluxes that the spacecraft is being subjected to during SEP events and in the presence of other sources of radiation such as the Earth radiation belts.

5.1 Bow-tie Analysis

5.1.1 Method

The count rate measured by BERM in each channel is related to the local particle flux, $\phi(E)$ according to equation 5.1.

$$R_{ch} = \int_0^\infty \phi(E) F_R(E) dE \tag{5.1}$$

Where F_R is the channel's response function in cm^2·sr (geometric factor).

The bow-tie inversion technique, firstly introduced by Van Allen [26] and used by several authors (e.g. [27] [28]), is used to unfold $\phi(E)$ from observations for channels whose response functions do not have ideal boxcar or step-like shapes. This technique allows to determine the effective geometric factor (G_{eff}) and the effective energy (E_{eff}) of BERM's channels. The method assumes that the encountered energy spectra ($\phi(E)$) is described by power laws $\phi(E) \sim E^{-\gamma}$, with the spectral indices γ corresponding to a physically reasonable range that is likely to be observed by the instrument. This suits the needs concerning BERM, given that it is expected that it measures mostly solar energetic particles, which usually follow a power law distribution in terms of their energy spectra.

The E_{eff} and G_{eff} of a channel are related to each other, to its count rate and to the incoming flux according to equation 5.2 or 5.3, depending on whether the channel is differential or integral, respectively.

$$\phi(E_{\text{eff}}) = \frac{R}{G_{\text{eff}}} \quad [\text{s}^{-1} \cdot \text{sr}^{-1} \cdot \text{cm}^{-2} \cdot \text{MeV}^{-1}] \tag{5.2}$$

$$\phi(E > E_{\text{eff}}) = \frac{R}{G_{\text{eff}}} \quad [\text{s}^{-1} \cdot \text{sr}^{-1} \cdot \text{cm}^{-2}] \tag{5.3}$$

For each channel, the goal of the bow-tie analysis is therefore to determine the effective geometric factor and energy. The method consists of plotting a family of G(E) curves that describe the relation between the characteristic geometric factor and characteristic energy: equations 5.4 (differential channels) or 5.5 (integral channels).

$$GdE(E) = \frac{\int_0^\infty \phi(E')R(E')dE'}{\phi(E)} \tag{5.4}$$

$$G_I(E) = \frac{\int_0^\infty \phi(E')R(E')dE'}{\int_E^\infty \phi(E'')dE''} \tag{5.5}$$

Each curve is plotted considering an energy spectrum that follows a power law, $\phi(E) \sim E^{-\gamma}$, with a different spectral index γ. The spectral indices were considered to be in the interval $\gamma \in [1.5, 3.5]$, corresponding to interval of spectral indices of solar energetic particle spectra that BERM is expected to encounter.

The plotted family of curves form a bow-tie shape (see top of figure 5.1) after which the technique is named, and the desired solution (E_{eff},G_{eff}) lies at its knot, where the solution is the same independently of the spectra index.. The channels' responses are not ideal: phenomena such as particle scattering blur the edges of the response in a real detector. For that reason, the knots in the bow-tie diagrams do not have a null thickness. The effective energy is determined by minimizing the standard deviation of the $\{\gamma, G(E, \gamma)\}_E$ distribution at each given energy, normalized to the mean of the distribution (see bottom of figure 5.1). The determined E_{eff} is assumed to be exact, whereas the G_{eff} is considered to be the mean of the distribution $\{\gamma, G(E, \gamma)\}_{E\text{eff}}$, with negative and positive uncertainties corresponding to the 5th and 95th percentiles subtracted by that mean.

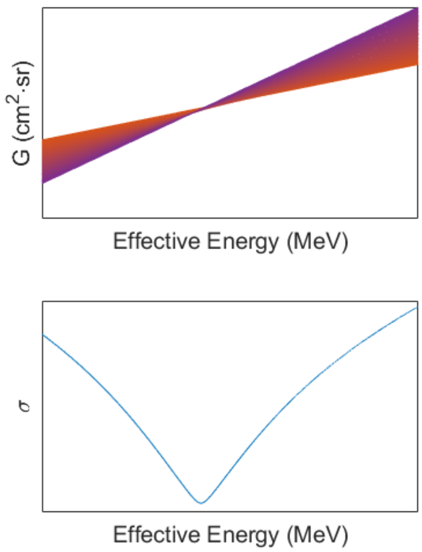

Figure 5.1: Example of a bow-tie shape, obtained by convoluting modeled spectra ($\phi(E) \sim E^{-\gamma}, \gamma \in [1.5, 3.5]$) with the response function of one of BERM's bins.

5.1.2 Results

The bow-tie method, as previously described, was applied to the geometric factors presented in sections 4.2.1 and 4.2.2. Obtaining the channels' effective geometric factors ($G\delta E$ for differential channels and G_I for integral ones) and effective energies (E_{eff}) will allow to convert BERM's counts into particle flux units. All bins that seem to exhibit the capability to perform measurements regarding a particle type that doesn't correspond to the one they were designed to measure (i.e. EP, HP and PE bins) are also included in this analysis.

5.1.2.A Incident Protons

Proton Channels

The results from the bow-tie analysis on the geometric functions of the proton bins, P1 to P8 (see figure 4.5) can be found in figure 5.2 and in table 5.1.

Channel	Channel Name	Type	E_{eff} (MeV)	GdE (cm^2·sr·MeV)	G_I (cm^2·sr)	σ_{min}	δ_G^-		δ_G^+	
6	P1	Dif	2.73	2.23E-03	-	0.086	-1.97E-04	-9%	3.62E-04	16%
7	P2	Dif	13.46	8.25E-03	-	0.189	-1.62E-03	-20%	3.01E-03	37%
8	P3	Dif	7.36	1.47E-03	-	0.013	-2.11E-05	-1%	3.72E-05	3%
9	P4	Dif	17.65	3.62E-03	-	0.021	-8.35E-05	-2%	1.40E-04	4%
10	P5	Dif	29.22	1.34E-02	-	0.029	-4.17E-04	-3%	7.13E-04	5%
11	P6	Int	27.17	-	3.91E-04	0.019	-1.38E-05	-4%	8.44E-06	2%
12	P7	Int	47.23	-	3.63E-04	0.015	-1.00E-05	-3%	6.03E-06	2%
13	P8	Int	70.6	-	4.63E-04	0.009	-8.11E-06	-2%	4.82E-06	1%

Table 5.1: Characteristic energies and geometric factors of proton channels of BERM (P bins). E_{eff} corresponds to the minimum value of the normalized standard deviation σ of of the $\{\gamma, G(E,\gamma)\}_E$ distribution. G or G_I correspond to the mean value of $\{\gamma, G(E,\gamma)\}_{E_{\text{eff}}}$, and the errors δ_G^- and δ_G^+ correspond to the fifth and ninety-fifth percentile of the distribution subtracted by the mean value.

All graphs exhibit a clear bow-tie shape, despite their non null thickness. Out of all the 8 proton bins, P2's bow-tie has the greatest thickness - supported by its value of σ_{min} being the largest - and it is also the one where the σ distribution is visibly more round when close to the minimum value (see bottom plot of figure 5.2b). This means that not only the the effective geometric factor will have a greater associated error (corroborated by these columns in table 5.1) but also that the effective energy would have a greater error, if these had been determined. To note that no errors were attributed to the effective energy due to the complexity of determining a statistically reliable criterion to do so, which should be addressed and solved in future work.

To evaluate the effectiveness of the method, three worst-case SEPs (worst-week 1989, worst-day 2000 and 2003) from the Radiation Hardness Assurance processed defined in the European Cooperation for Space Standardization guidelines were used. This test consists of simulating an encounter between BERM and the event, through the convolution of the response function (F_R) of the first, with the spectrum ($\phi(E)$) of the second, as described in equation 5.1. The spectra of these events were obtained in OMERE 5.6, a radiation environment and effects engineering tool developed by TRAD (that

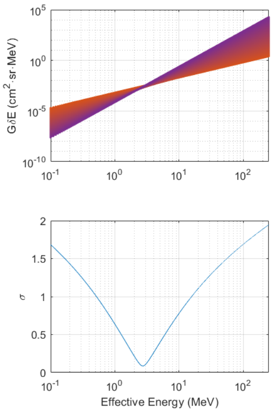

(a) Proton bin 1.

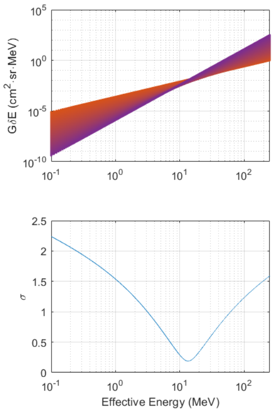

(b) Proton bin 2.

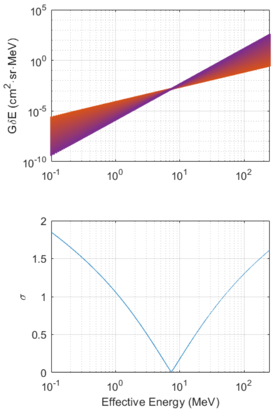

(c) Proton bin 3.

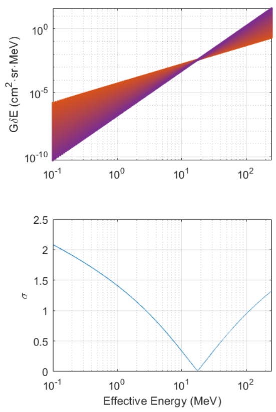

(d) Proton bin 4.

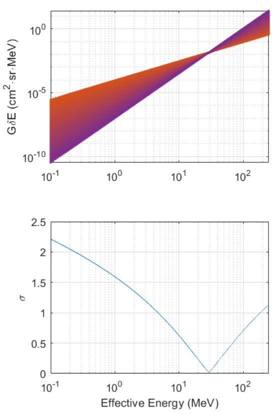

(e) Proton bin 5.

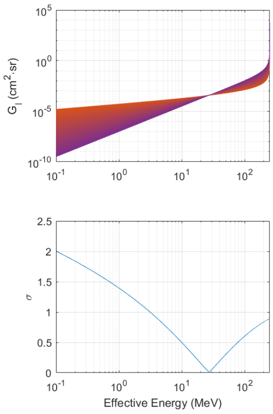

(f) Proton bin 6.

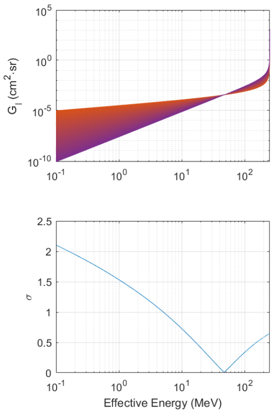

(g) Proton bin 7.

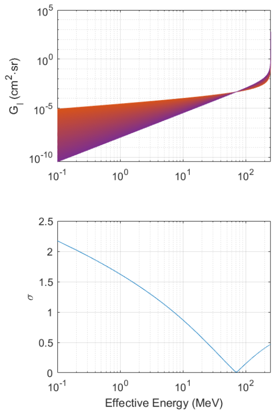

(h) Proton bin 8.

Figure 5.2: Graphs resultant from the bow-tie analysis of the proton bins' geometric factor (P1 to P8 in figure 4.5). For each proton bin, the top graph shows the said bow-tie, formed by the several curves described by equation 5.2 (differential) or 5.3 (integral), considering exponential spectra $\phi(E) \sim E^{-\gamma}, \gamma \in [1.5, 3.5]$. The bottom plot shows the standard deviation of the $\{\gamma, G(E,\gamma)\}_{E_{\text{eff}}}$ distribution, divided by the mean value of that distribution.

can be downloaded at https://www.trad.fr/en/download/). The count rate that, according to the convolution, would be registered by BERM is then reconverted to flux units, using the results of the bow-tie analysis from table 5.1. The obtained fluxes were compared to the values from the initial spectra for each correspondent energy. The results are shown in figure 5.3. As it can be seen, the method is successful in obtaining the initial particle flux for each channel with the exception of P2. Note that, as a result of the response functions, P2 has the third largest characteristic energy for protons (third data point, in the top graphs). In all three events, the real flux for the characteristic energy of P2 sits outside the interval of uncertainty of the reconstructed flux. This fact agrees with previous comments regarding the thickness of its bow-tie, hinting that the bow-tie method might not be suited for the geometric factor's curve of P2. Table 5.2 summarizes how adequately the reconstructed fluxes relate to the respective spectra curves.

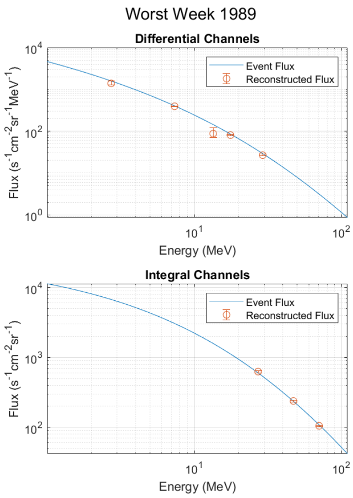

(a) Energy spectrum of protons during a solar flare event in 1989.

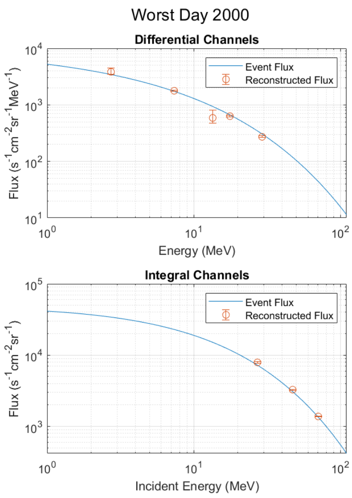

(b) Energy spectrum of protons during a solar flare event in 2000.

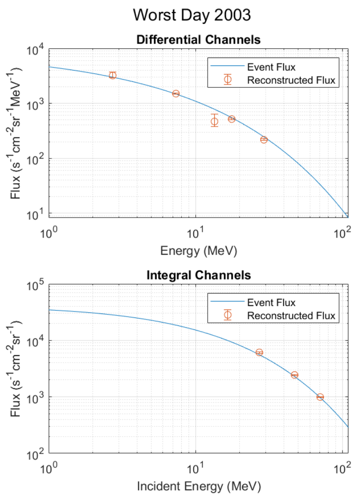

(c) Energy spectrum of protons during a solar flare event in 2003.

Figure 5.3: Graphical representation of the reconstruction of fluxes by simulating an encounter between the three events with BERM. The lines in blue represents the real spectrum of the event consulted in OMERE 5.6, consisting of a .txt file with 3 columns of discrete data: energy, differential flux and integral flux. The points in red are the reconstructed fluxes from BERM's count rate using the effective energies and geometric factors. Each red data point corresponds to one proton bin.

Event	χ^2/ndf	χ^2/ndf (without P2)	$(\phi_{event}/\phi_{recv})_{P2}$
1989	7.76	4.03	1.64 $\pm$ 0.40
2000	29.75	11.09	1.60 $\pm$ 0.45
2003	26.31	6.15	1.67 $\pm$ 0.42

Table 5.2: Parameters related to goodness of fit of the graphs in figure 5.3.

The χ^2/ndf value for the event of 1989 is in the order of magnitude of 1, which is a satisfactory goodness of fit test result. For the 2000 and 2003 events these values are greater than desired, when P2 is included. If P2 is excluded these values improve greatly, confirming that the bow-tie method is appropriate for the rest of the channels and produces reliable results. From the third column of table 5.2 it is possible to see that the ratio between the real flux for E_2^{eff} and the reconstructed one is approximately constant for all events. In this case, a conversion factor $CF_2 \approx 1.63 \pm 0.43$ may exist such that the effective geometric factor of P2 is being underestimated and if the effective geometric factor to be used in the data analysis is $G\delta E_2' = \frac{G\delta E_2}{CF_2}$ it will yield more reliable results than using the value resultant from the bow-tie analysis.

Upgraded P3 channel

In events in which heavy ions are not present, protons that should be attributed to channel P3 will be responsible for all the counts in channel HI1, (see figure 4.6b and respective discussion). For such events, it is useful to know the characteristic energy and geometric factor of channel P3 summed with the peak in the response function of HI1, because the counts in these two channels can also be summed. The result is presented in table 5.3. The analysis in figure 5.3 was repeated for the upgraded P3 bin and table 5.4 shows the obtained χ^2/ndf and a comparison with the previous value (in table 5.2). Despite being small, there are improvements (χ^2/ndf is closer to 1) for the whole set of channels, meaning that the improvement in the channel P3 alone is not negligible. For that reason, for events where heavy ions are not present, and all the counts in channel HI1 are therefore due to protons, this upgraded channel should be used instead of the single channel P3. Note however that the response of BERM to heavy ions has not been studied yet. Also, a change in the LUT could also be done to attribute proton events from HI1 to P3.

Channel	Channel Name	Type	E_{eff} (MeV)	GdE (cm^2·sr·MeV)	σ_{min}	δ_G^-		δ_G^-	
8 + 14	uP3	Dif	7.51	1.80E-3	0.011	-3.29E-5	-2%	5.94E-5	3%

Table 5.3: Characteristic energy and geometric factor of BERM's P3 summed with HIP1 to tackle the fact that protons are incorrectly attributed to HIP1.

Event	χ^2/ndf (without P2)	Improvement
1989	3.75	7%
2000	9.77	12%
2003	5.28	14%

Table 5.4: Comparison of the χ^2/ndf parameter between the test performed in 5.3 and the same test repeated for upgraded P3 channel.

Electron Channels as Proton Channels

Given that the electron channels are also sensitive to protons (see figure 4.6a) it makes sense to perform the bow-tie analysis on these channels as well. However, they should only be used when no electrons are present in the event (or if their relative presence is negligible). Channels EP1 and EP2 have two regions of high sensitivity: one for protons of ~ 1 MeV and other for protons > 100 MeV. For the performed bow-tie analysis, only the first region in each was analysed. The decision of analysing these regions alone relies on the usefulness of these channels for events where high energy protons are absent. When high energy protons (> 100 MeV) are present, bins EP3 to EP5 can provide information free of contamination by low energy protons, unlike EP1 and EP2. For that reason there would be no added value in performing the analysis on the whole geometric factor for these two bins.

The results obtained can be found in table 5.5, with the caveat that, due to their high sensitivity to energetic protons, the values for channels EP1 and EP2 can only be used when the event at hand does not exhibit fluxes of protons higher than 80 MeV.

Channel	Channel Name	Type	E_{eff} (MeV)	GdE (cm^2·sr·MeV)	σ_{min}	δ^-_{GdE}		δ^+_{GdE}	
1	EP1	Dif	1.38	2.18E-09	0.001	-4.60E-12	-0.2%	7.44E-12	0.3%
2	EP2	Dif	1.44	3.87E-05	0.001	-4.18E-08	-0.1%	1.02E-07	0.3%
3	EP3	Dif	223.2	5.53E-02	0.010	-5.98E-04	-1%	1.05E-03	2%
4	EP4	Dif	228.72	8.48E-04	0.024	-2.22E-05	-0.04%	3.75E-05	0.1%
5	EP5	Dif	293.19	2.89E-03	0.004	-1.41E-05	-0.5%	2.44E-05	1%

Table 5.5: Characteristic energies and geometric factors of BERM's electron channels measuring protons (EP bins).

5.1.2.B Incident Electrons

Electron Channels

The results from the bow-tie analysis on the geometric functions of the original electron bins, E1 to E8 (figure 4.10) can be found in table 5.6 and in figure 5.4.

Channel	Channel Name	Type	E_{eff} (MeV)	GdE (cm^2·sr·MeV)	G_I (cm^2·sr)	σ_{min}	δ^-_G		δ^+_G	
1	E1	Dif	0.21	1.02E-08	-	0.033	-3.27E-10	-3%	7.46E-10	7%
2	E2	Dif	0.32	4.36E-05	-	0.029	-1.28E-06	-3%	2.67E-06	6%
3	E3	Int	0.35	-	8.53E-07	0.023	-1.00E-08	-1%	1.22E-08	1%
4	E4	Int	2.18	-	3.30E-07	0.023	-2.49E-08	-8%	1.43E-08	4%
5	E5	Int	1.63	-	7.87E-09	0.003	-7.18E-10	-9%	4.13E-10	5%

Table 5.6: Characteristic energies and geometric factors of electron channels of BERM (E bins, represented in figure 4.10).

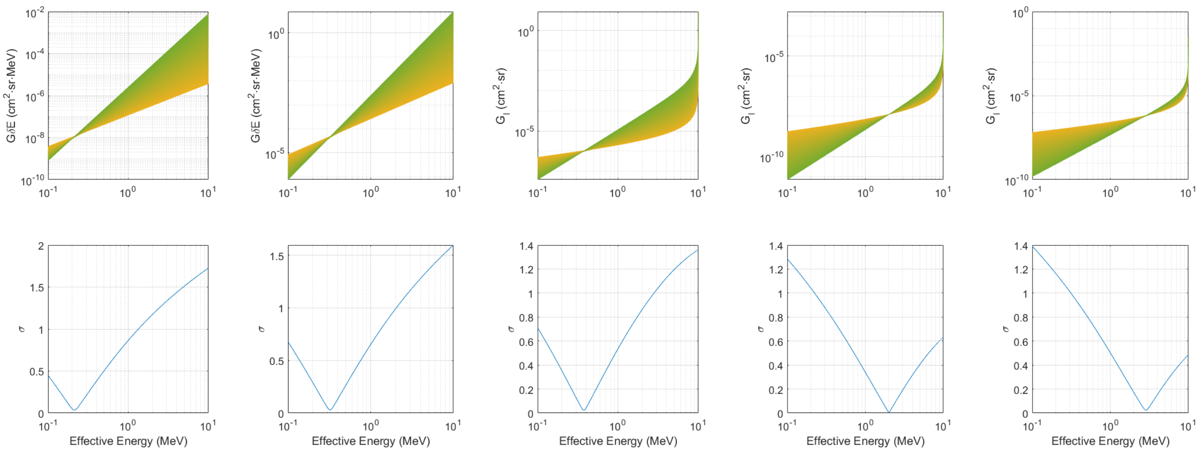

(a) Electron bin 1 **(b)** Electron bin 2 **(c)** Electron bin 3 **(d)** Electron bin 4 **(e)** Electron bin 5

Figure 5.4: Graphs resultant from the bow-tie analysis of the electron channels' geometric factor of BERM (E bins, see figure 4.10).

All channels have tapered σ curves that reach a very low σ_{min}, which is also reflected in the reduced errors (δ^+ and δ^-) that never exceed 10%.

Similarly to the analysis done for protons, the results of the bow-tie analysis for electron bins was tested by convolution of the response functions with the spectrum of the solar event that happen in

November 2nd of 2003. This spectrum was not composed of discrete data, but it was instead a continuous function that resulted form a fit to experimental data points [3]. The result of the test is represented in figure 5.5. For both differential and integral channels the respective fluxes are reconstructed accurately. The reconstructed values are always within 10% of the real ones.

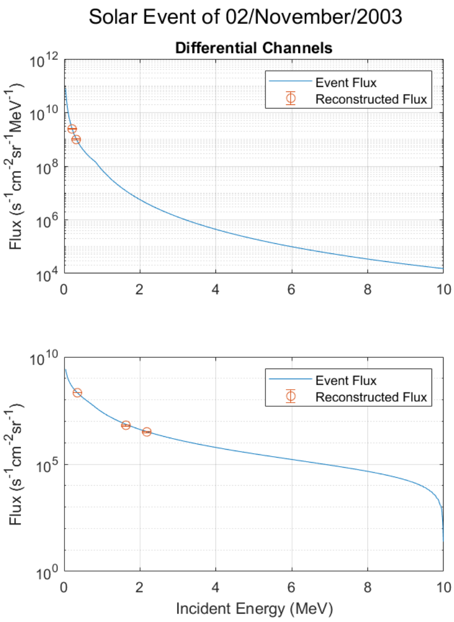

Figure 5.5: Graphical representation of the reconstruction of fluxes by simulating an encounter between BERM and the solar event of November 2^{nd} 2003 (see figure 5.6).

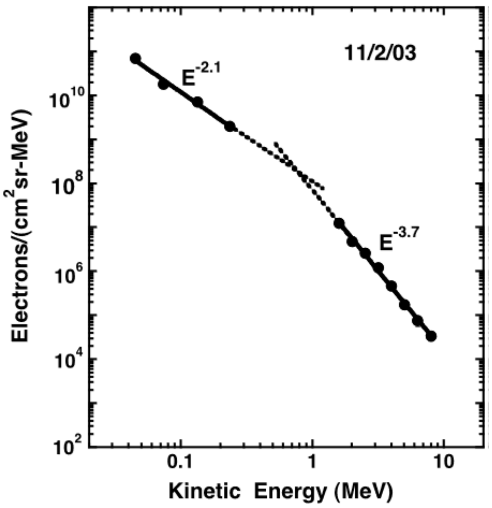

Figure 5.6: Real energy spectrum of the solar event of November 2^{nd} 2003 that was the basis for the computed flux used in the test of figure 5.5. From [3].

Channel E4 and E5 were included in this study, and it seems that the bow-tie analysis is appropriate to the shape of their geometric factor - as confirmed by its low σ_{min}, reduced errors and the successful reconstruction of the original fluxes in 5.5. However, due to the channels' previously mentioned low statistics, it is unclear whether the use of their effective energies and geometric factors will yield reliable results.

Proton Channels as Electron Channels

Given that the proton channels are also sensitive to electrons, the bow-tie analysis was performed for PE channels 6, 7 and 10. The results can be found in table 5.7. These channels can be interesting for events in which protons are not present, such as electron bursts detected in mercury's magnetosphere discussed in section 2.3.1.

Channel	Channel Name	Type	E_{eff} (MeV)	G_I (cm^2·sr)	σ_{min}	δ_G^-		δ_G^+	
6	PE1	Int	0.29	3.06E-06	0.018	-9.74E-08	-3%	6.72E-08	2%
7	PE2	Int	0.47	1.16E-06	0.031	-3.91E-08	-3%	7.19E-08	6%
10	PE5	Int	1.91	8.70E-07	0.006	-5.86E-09	-1%	9.72E-09	1%

Table 5.7: Characteristic energies and geometric factors of BERM's proton channels measuring electrons (PE bins, represented in figure 4.11).

5.2 BERM Flight Data Analysis

Since BepiColombo's took off, BERM has collected data from the flybys to Earth, Venus and Mercury, as well as from the percentage of the cruise phase that happened so far. Up to date, 17 solar particle events have been registered by BERM. Two of them are worthy of special attention.

The first event to be studied happened in February 8$^{\text{th}}$ 2022. It was the first event that caused a relevant signal in all 8 proton channels and on 3 of the electron channels. The described study of this event represents an opportunity to show how an event is analysed and what kind of conclusions the results of the bow-tie method allow to draw about it.

The second one happened in April 17$^{\text{th}}$ 2021. This one was selected because the other particle spectrometer of the MPO, the SIXS-P [10], was also in operation. As mentioned before, SIXS-P has an energy range that overlaps with BERM's. Performing a comparison between the fluxes measured by the two instruments allows to validate the bow-tie analysis performed for BERM.

5.2.1 Earth Flyby by BepiColombo - Channel E1 problem

During the development of this work, the data collected during BepiColombo Earth's flyby were being analysed in parallel using the results of the bow-tie analysis discussed in the previous section. One of the main findings of that analysis, that is relevant for this work, was that the flux computed by channel E1 was $\sim$10^3 greater than expected.These measurements are relative to the outer belt (dominated by electrons) and this difference cannot therefore be fully explained by proton contamination. Given that the flux is calculated according to equation 5.2, such a large overestimation of the flux indicates that E1 is registering much more counts than predicted by the current response function. There are two possible origins to this difference. One is that the geometric factor of E1 may have a greater magnitude than the one in figure 4.10, meaning that its effective geometric factor (currently $\sim 10^{-9}$cm^2·sr·MeV) is being underestimated. A possible reason for this could be the overestimation of detection trigger threshold value, whose current value is responsible for the low geometric factor magnitude verified in this channel, as discussed in section 4.2.2. Another possible origin for the overestimation of counts in channel E1 could be related to the associated electrons such as cross-talk between the detectors or noise.

5.2.2 Analysis of SEP Events

BERM in-flight data is gathered and made available in FITS files. Each file corresponds to a 24 hour period, integrated into 30 seconds intervals. The resulting ASCII data table is therefore displayed in twenty four columns and 2880 lines (if BERM is functional for the whole day). The first three columns identify date and time in different formats, whereas the fourth one identifies BERM's operating mode. The remaining columns are related to particle detection: the fifth column corresponds to the total particle counter (total number of particles detected in that 30 second interval) and the following 18 correspond to the particle bins: 5 for electrons, 8 for protons and 5 for heavy ions. The last column corresponds to the vetoed events. The FITS files were analysed using MATLAB computing interface and language.

When radiation emitted by the Sun during solar events, such as as flares or a coronal mass ejections, is detected by BERM a spike occurs in the bins counters. However these counts still require some processing in order to be analysed, as illustrated in figure 5.7. The first step of the processing consists of determining the background rate, e.g. due to galactic cosmic rays, in order to remove it. For each channel the total number of counts during the 2 to 5 five days prior, are converted to rates and considered as the background value for that channel. After converting BERM's counts to count rates, these are averaged over any desired time interval, and the previously determined background rates are removed. Finally the count rates are converted to fluxes according to equations 5.2 and 5.3.

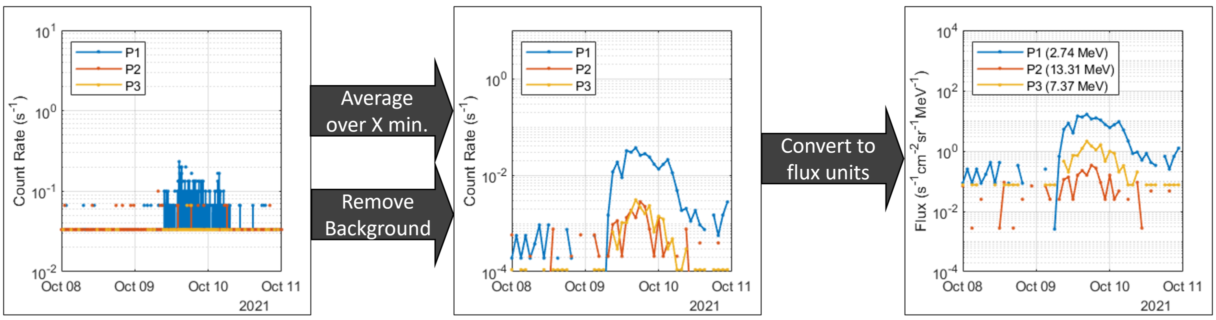

Figure 5.7: Pictorical description of the processing of data for SEP analysis. For the specific event depicted in this figure, the data were averaged over 90 minutes.

5.2.2.A SEP event of February 8th 2022

The count rates observed by BERM's channels can be found in figures 5.8 (electron channels) and 5.9 (proton channels). Concerning figure 5.8, Channel 4 and 5 are not present because they did not register any signal above the noise levels, meaning that the event was short on electrons on the order of 1 MeV and above (see table 5.6), but also on protons above 220 MeV given that these channels would be sensitive to them (see table 5.7). The fact that channel 3 has such a clear signal allows to state with certainty that the event was rich in electrons, given that this channel is not be contaminated by low energy protons (unlike channel 1 and 2). The fact that electrons exist does not allow that channel 1 and

2 are treated as EP bins. However, one can observe that the the temporal evolution of the signals in channels 1 and 2 are different from the one in channel 3. This is probably not fully explained by the fact that channel E3 is integral while the other are differential. The evolution in channel 1 and 2 are in in fact very similar to the one of the signal in channel 6, indicating that there is contamination by low energy protons (1.0-2.0 MeV) in channels 1 and 2, which would be expected, given their sensitivity to these.

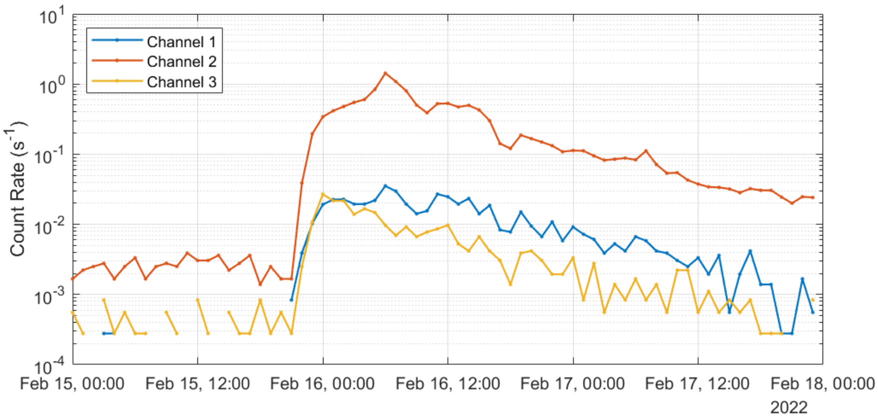

Figure 5.8: Count rate in the first 3 electron channels by BERM during the event of February 8th 2022. The fact that there are counts registered in channel 3 indicates that electrons exist and these channels must be treated as E channels.

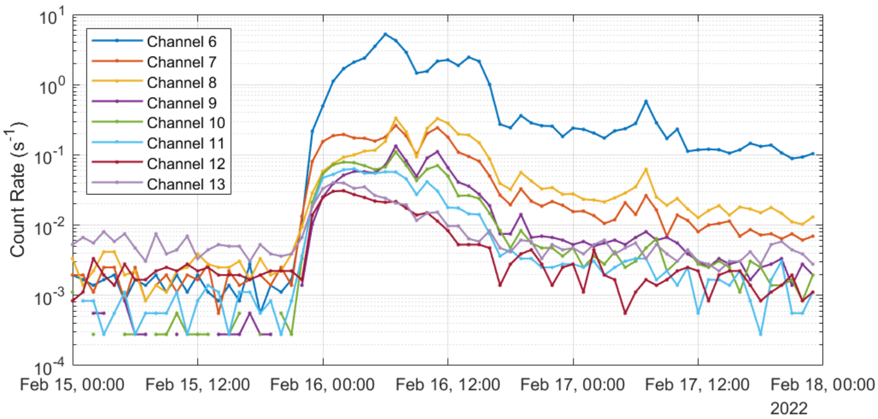

Figure 5.9: Count rate registered in the 8 proton channels by BERM during the event of February 8th 2022.

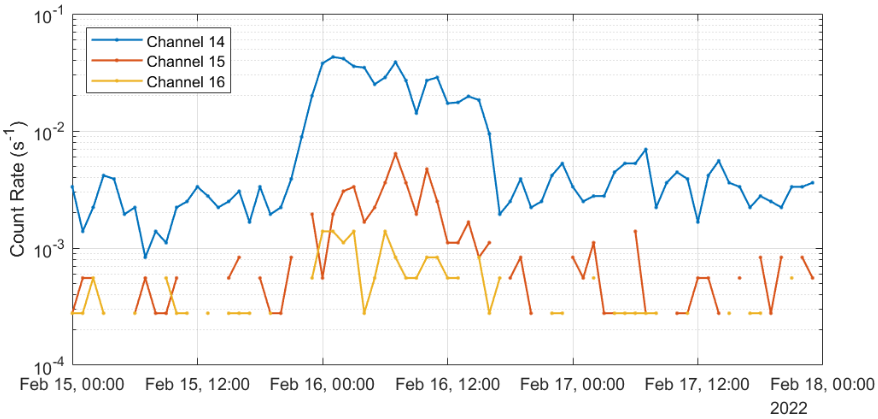

Figure 5.10: Count rate registered in the first 3 heavy ion channels by BERM during the event of February 8th 2022.

The comparison of the temporal evolution of the signals provides information about the type of particles that were counted because different particles arrive at different times: electrons, due to lower mass, and high energy electrons, due to highest velocity, will reach BepiColombo before lower energy protons.

It is expected that the count rates in the proton channels (figure 5.9) are all due to incident protons. On the other hand, in figure 5.10 shows that the temporal evolution of the count rate in channel 14 is very different from the one in channel 8. When combined, these two form the altered P3 channels discussed in section 5.1.2.A, however, in this case it is not clear that the signal in channel 14 is due to protons. A deeper study on the time of arrival of the protons that HIP1 is sensitive to is required to understand whether these counts are due to protons or to heavier ions. Until further studies are conclusive, the two channels shall not be combined.

Figures 5.11 and 5.12 show the electron and proton count rates converted to fluxes, using the effective geometric factors in tables 5.6 and 5.7, respectively. According to figure 5.11, the flux measured by E1 is 1000x higher than the one measured in E2. This is unlikely to represent reality, given the close proximity of the effective energies of the two channels: it results from the fact that the fluxes in channel E1 are being highly overestimated, as discussed in section 5.2.1.

In figure 5.12, the fluxes measured by the differential bins seem to exhibit a behaviour according to expected: the higher the characteristic energy of the channel, the lower its flux. However, this is not true for the flux measured by P2 (13.31 MeV), that presents itself extremely close to P4's. This results from the already discussed inadequacy of the bow-tie analysis for the P2 geometric factor. The fact that the two flux values are very similar is actually in agreement with the result in figure 5.3, where for the 3 tested events is possible to see that the reconstructed flux for P2 (third data point) is very close to the one for P4 (17.53 MeV, correspondent to the fourth data point). The fact that this proximity is present both in figure 5.3 and in the measured data confirms that, contrary to what happens for E1, the problem results from the bow-tie analysis itself, and not from a misinterpretation of reality. Figure 5.12 also includes the

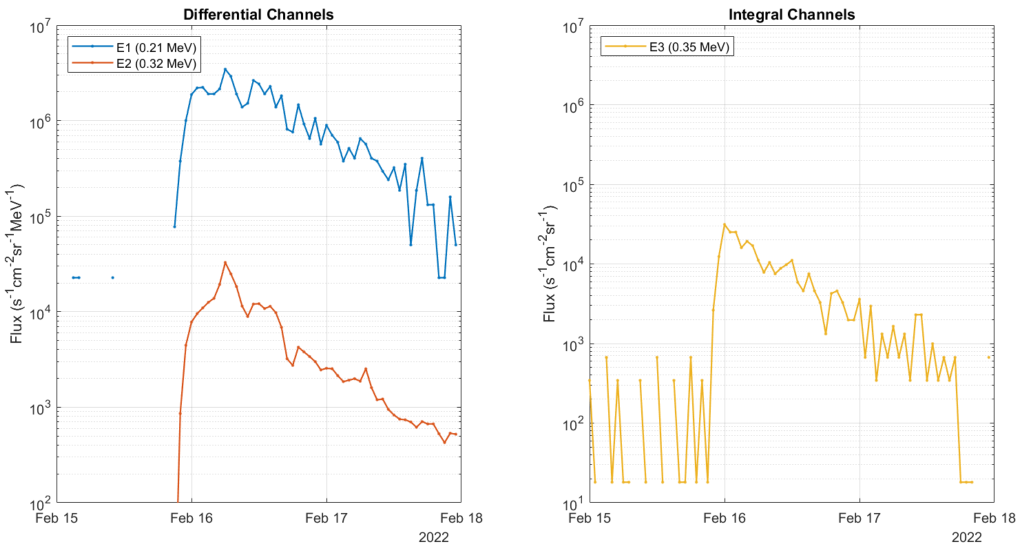

Figure 5.11: Fluxes registered by BERM in the first 3 electron bins during the event of February 8th 2022, using the results of the bow-tie analysis.

curve for P2 considering the conversion factor CF_2 introduced in section 5.1.2.A.

Although it is not a goal of this work to characterize the events itself, it is useful to understand what conclusions can be drawn. For that purpose, a power law curve was fitted to the set of points $(E_{\text{eff}}, \phi(E_{\text{eff}}))$ at each moment in time, in order to understand if indeed the spectrum of this event is compatible with a power law and also to understand how the spectral index varies or if it is stable. Figure 5.17 shows the result of these fits, for all differential bins including P2 (referred to as SET 1), and excluding P2 (SET 2), and including P2 with the conversion factor (SET 3). The Root Mean Squared Error (RMSE) of the fits (figure 5.13a) starts high and variable at the beginning of the event, this is expected given that at the beginning of the event the spectra is not as stable, due to contamination with high energy protons and/or electrons that arrive first. However the RMSE stabilizes and approaches 0 as the event unfolds, as expected. The RMSE evolution is always further away from zero for SET 1, than for SET2, which in turn is always further away from zero than SET3. This confirms that the presence of P2 disturbs the exponential behaviour of the energy spectrum. On the other hand, the use of conversion factor CF_2 represents an improvement once the energy spectra "stabilizes" - around 00:00 of February 17.

To determine whether the spectrum of the event can be successfully reconstructed, the spectral index γ must also be studied. The fits in figure 5.13b yields a γ(t) that, after stabilizing on 00:00 of April 17, oscillates around $\gamma = 2$, in the interval $\gamma \in [2 - 0.3; 2 + 0.3]$. These oscillations, however, seem random, indicating that they probably result from the fact that the exponential fit is done to only 4-5 points, which is not a large enough set to produce stable enough fits. Although with an associated error, it is possible

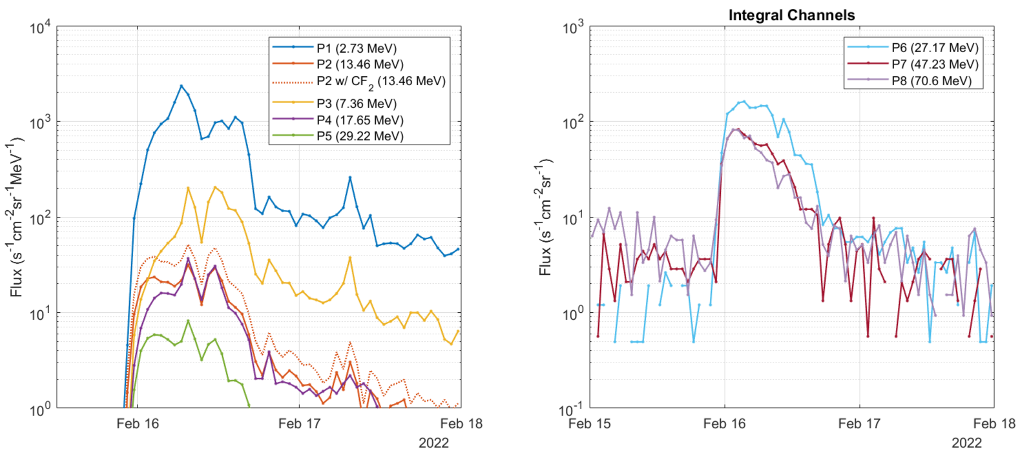

Figure 5.12: Fluxes registered by BERM in the 8 electron bins during the event of February 8th 2022, using the results of the bow-tie analysis.

to estimate the spectral index of the event, showing the validity of the method, if a power law spectrum is considered.

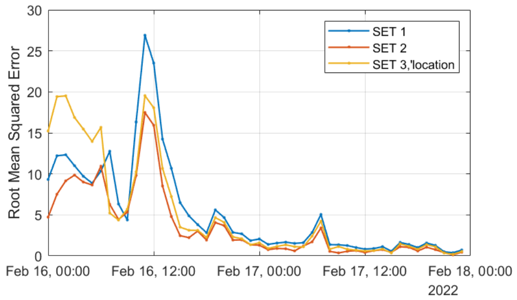

(a) Root mean squared error of the fit.

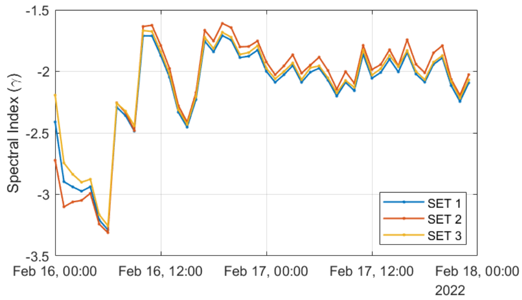

(b) Spectral index of the event.

Figure 5.13: Results of fit a power law to the data points $(E_{eff}, \phi(E_{eff}))$ correspondent to differential channels, at each moment in time of the event of February 8th 2022.

5.2.2.B SEP event of April 17th 2021

On April 17th 2021 BepiColombo observed a Solar Energetic Particle event. Both BERM and SIXS were in operation and detected the event, which allows to compare the measurements between SIXS-P and BERM.

The fluxes measured by BERM proton channels that have signals above the noise levels are presented in figure 5.14. As it can be seen, the fluxes decrease with increasing energy, with the exception of P2, whose flux is very similar to P4's and was therefore excluded from the joint analysis. The fluxes measured by both instruments are plotted together in figure 5.15. To note that SIXS-P bins P1 and P2 were not included in this analysis because they presented high electron contamination in the beginning of the event.

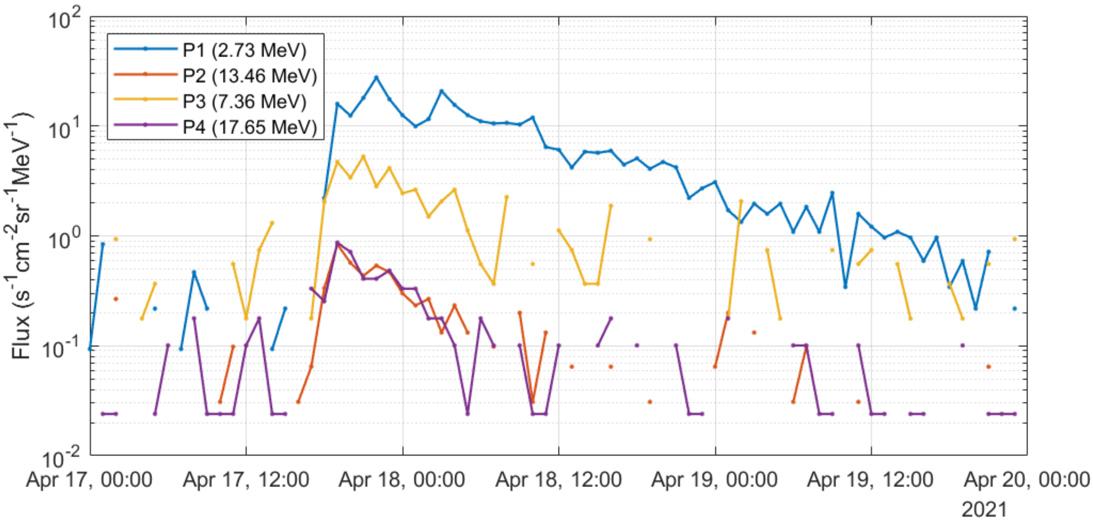

Figure 5.14: Proton fluxes registered by the first 4 proton bins of BERM during the event of April 17th 2021.

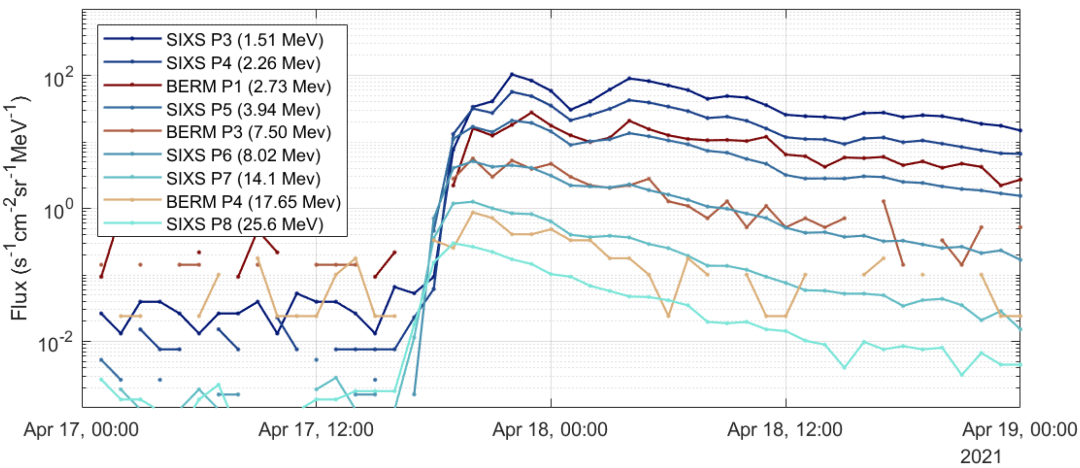

Figure 5.15: Proton fluxes registered by BERM and SIXS-P during the event of April 17th 2021.

The flux measured by BERM's P1 bin (1.51 MeV) lies between the respective SIXS channels that are right before and right after in terms of characteristic energies (1.19 MeV and 2.26, respectively). This also happens for BERM's P4 until April, 18 at 7:00, after which the count rate goes to background levels. The flux measured by P3 (7.5 MeV) matches the flux of SIXS P6 (8.02) MeV. Even though its characteristic energy is slightly lower this can be explained by the fact that the pointing directions of both instruments are not the same.

To compare the fluxes of measured by the two instruments, and similarly to what was done in the previous event, a power law curve ($\sim$E$^{-\gamma}$) was fitted the set of points $(E_{eff}, \phi(E_{eff}))$. Three fits were performed, one for BERM alone, one for SIXS-P alone and one for the measurements of the two instruments together. Figure 5.16 shows one example of the fitted spectra. Figures 5.17a and 5.17b show, respectively, the time evolution of the spectral index γ and of the root mean squared error of these fits.

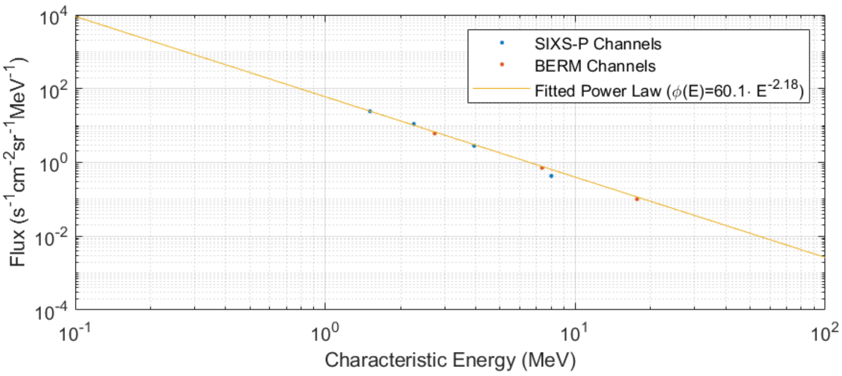

Figure 5.16: Power law fitted to the data points $(E_{eff}, \phi(E_{eff}))$ of BERM and SIXS-P at 12:00 of April 18th.

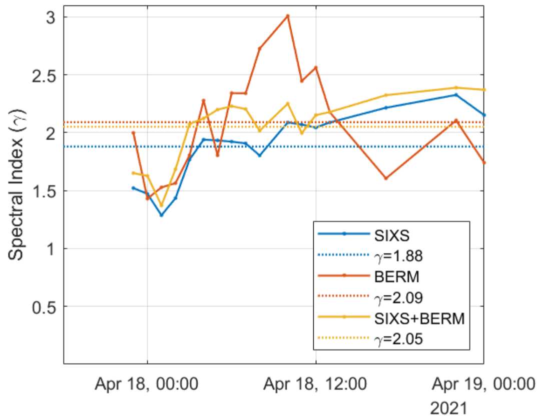

(a) Spectral index extracted from the fits. Dashed lines correspond to the mean spectral index for each curve.

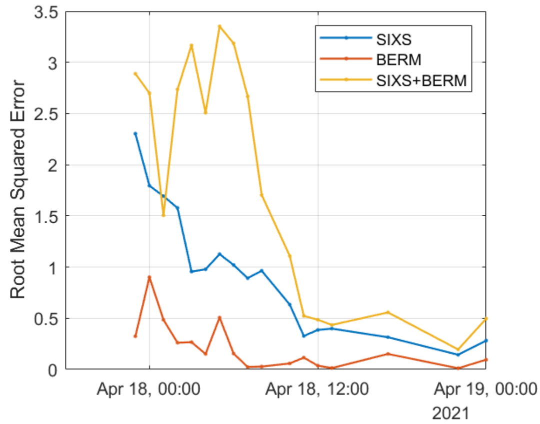

(b) Root mean squared error of the fits.

Figure 5.17: Results of fit a power law ($\sim E^{-\gamma}$) to the data points $(E_{eff}, \phi(E_{eff}))$ correspondent to differential channels, at each moment in time of the event of April 17th 2021.

The RMSE is low for (< 3.5) for the three fits. One negative aspect that can be observed is that the RMSE for the fit where the two instruments are considered together is always greater than for the fits where each one is considered alone. However, it is important to note that the fluxes measured by the two instruments do not have to perfectly complement each other given that they are not measuring the flux at the exact same point in space and if the flux is not isotropic, slight spatial differences may occur.

The dashed lines in figure 5.17a illustrate around what mean value, each of the curves oscillate, between the mean value for SIXS-P alone and BERM there is a difference of 11%. Given that BERM's curves are fitted to only 3 points, although apparently satisfactory, this result must be interpreted with caution.

Figure 5.18 shows the electron flux measured by E2. These counts are assumed to be originated by mostly electrons, although proton contamination is likely to have occurred. The criterion, was again the time evolution of the curve that differs from the proton channels (both from BERM and SIXS) and is actually similar to the evolution observed in SIXS-P electron channels. For that reason, they were plotted together, in figure 5.19, where it is possible to see that the flux registered BERM E2 bin lies between SIXS-P's E4 and E5, as expected given that its characteristic energy is also between the characteristic energies of those SIXS channels.

No fits were performed to the curves because BERM would only contribute with one of the total 6 data points. Clearly the fit would be dominated by SIXS-P's data points and it wouldn't add any conclusion of value to this analysis.

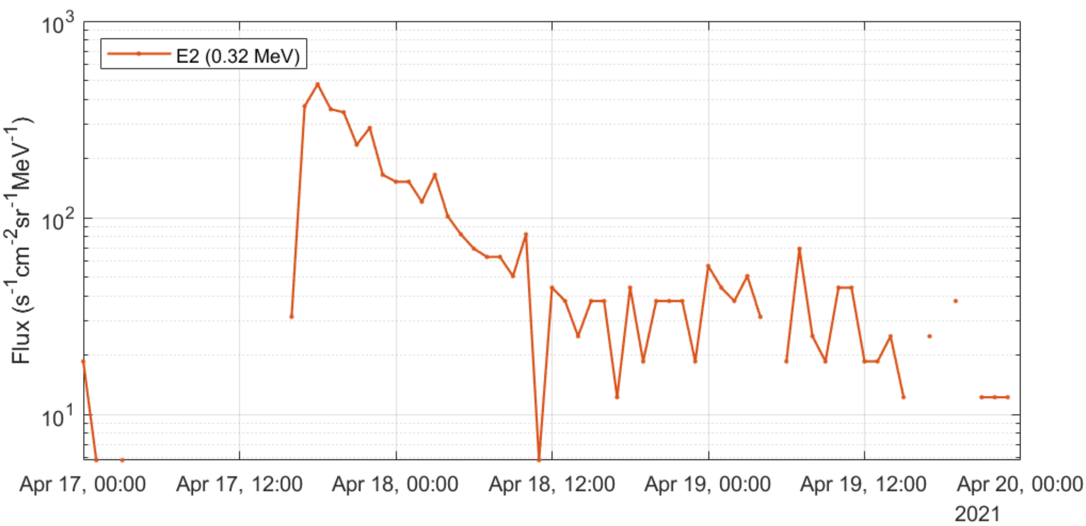

Figure 5.18: Electron flux registered by BERM in the second electron bin during the event of April 17th 2021, using the results of the bow-tie analysis.

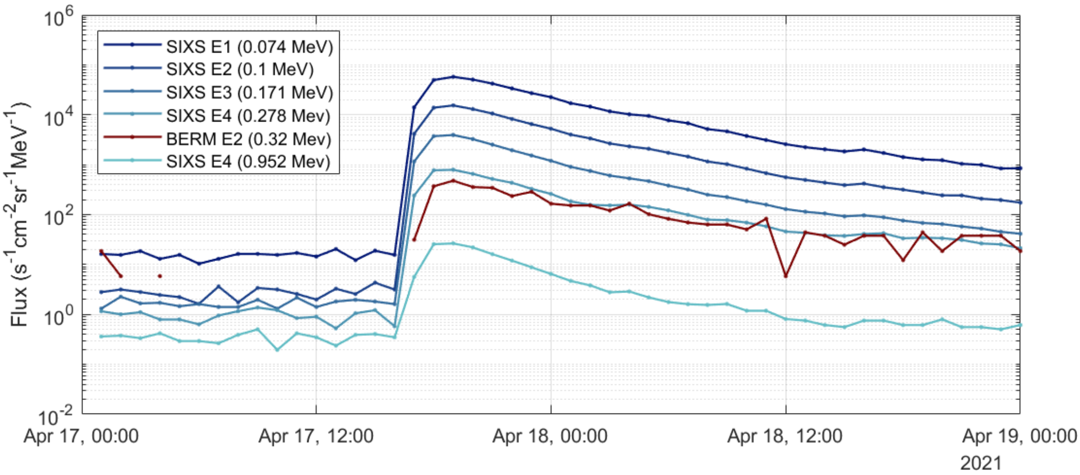

Figure 5.19: Electron fluxes registered by BERM and SIXS-P during the event of April 17th 2021.

Despite the discussed imperfections in the comparison, the fluxes measured by the two instruments are clearly related, which allows to attest that the fluxes obtained from BERM data using the bow-tie method described in this work are indeed reliable.

6

Conclusion

Contents

In this work, the response of the BepiColombo Radiation Monitor to electrons and protons was studied in order to reliably analise flight data.

In the first part of this thesis, the particle reconstruction algorithm of BERM was revisited and implemented in C++ in order to obtain the response functions. The main characteristics of the detector response were studied in order to comprehend its behavior in flight.

In the second part of this work, a method to convert BERM's raw data (counts) into physical units was developed. The method adopted to perform this task was the bow-tie method, which assumes an incident power-law energy spectra ($\phi(E) \sim E^{-\gamma}, \gamma \in [1.5; 3.5]$). Using this method, the pairs of effective energy and flux for each channel (for both electrons and protons). The validity of the method was tested against SEP models. All channels showed good results with the exception of P2 and E1. These results were already applied to analyse the data of the BepiColombo's flyby to Earth, even though the spectra in the belts is not fully represented by a power law [29]. This is the main fragility of the method: assuming these fixed mathematical functions to describe the spectral behaviour makes it less robust and universal. Even when the form of the spectra is not described by a power law, the obtained fluxes will be skewed in the direction of fitting one, possibly leading to misinterpretations. Nevertheless, it is a first approach to the issue of obtaining flux spectra from BERM, which was impossible before.

Regarding the proton channels, the flux reconstruction is not successfully achieved for the P2 bin: the bow-tie method does not seem suitable for its geometric factor. This result was first hinted by the large error associated with the values determined for the channel effective energy and geometric factor, and was later confirmed by the test carried out using past event fluxes as well as by the reconstruction of fluxes detected by BERM during the cruise phase. In all encounters (simulated and real) the flux values determined for bin P3 were very close to those determined for P4. This is a positive factor as it confirms the similarity between simulations and reality, indicating that the geometric factor is a reliable representation of what is really happening. However, the data analysis is impaired by the method not being suitable for this bin. More detailed studies are thus required to solve this problem, because it is not certain that the conversion factor (CF_2) used is the most adequate. As for the remaining P bins, the results are positive: the bow-tie method seems to yield good results. The fluxes computed by bins P1, P3 and P4 are clearly related to those measured by SIXS-P in the event of April 17th 2021. This means that the proton fluxes measured in these channels as well in the other channels, with the exception of P2 are reliable enough to be used, and of particular importance when SIXS-P is not in operation.

Regarding electron detection in the electron channels, some issues are to be noted. The first one concerns the detection trigger threshold, which is estimated to be 220$\pm$24 keV (180$\pm$20 ADC). This value affects the detection of electrons greatly, because it is very similar to the energy deposited by these particles in the first detector. As discussed, the average energy deposited by electrons in detector 1 is always smaller than the current threshold value, meaning that the electrons, regardless of their energy, will trigger the detection system with low efficiency. Channel 1 is being particularly affected by the current trigger threshold value. Another problem is the lack of statistics to study the behavior of electrons that can cross the first 4 detectors and reach the fifth one. This makes it hard to state with confidence that the geometric factor of E4 and E5 correctly represent reality. Despite these problems, the bow-tie method seems to be adequate for the obtained geometric factor of the E bins. However, when analyzing the flyby data, it was verified that the reconstructed fluxes in E1 were about 1000 times higher than expected. This was confirmed by the study of SEP events registered by BERM: the flux measured in E1 was about 1000x higher than the flux measured in E2, which cannot be justified, given the proximity of their effective energies. This happens because E1 bin registers much more counts than predicted by its computed geometric factor, although the exact cause to this has yet to be understood. From the comparison with SIXS-P, the reconstruction of particle fluxes through the counts in E2 is accurate. The same can't be stated for bins E3 to E5 yet, because there were no SEP events to date where they registered a signal while SIXS-P was also in operation. In the case of channels E4 and E5 no significant signal were registered at all up to date - which is supported by the low statistics attributed to detectors 5-8, predicted by the simulation.

6.1 Future Work

The work that has been developed for this thesis brought up some questions, that require further studies to answer.

The first one concerns the detection trigger threshold. When the flight model of BERM was built, a replica - engineering qualification model (EQM) - was also built. Having this second model available is an asset, because it allows to perform an irradiation campaign designed to specifically determine the real trigger threshold value, which hasn't been done before. If the results of this campaign confirm the scenario that the current threshold value is overestimated, new response functions will have to be generated through a reanalysis of the Geant4 simulations, by taking into consideration the updated value. While these will affect the electron response functions, the same is not true for protons due to their higher stopping power. If the results of the campaign confirm that the current estimated value of 220 keV is correct, further studies must be performed to understand the origin(s) of the extra count rate in channel E1. The results will then be implemented into the simulations to improve the response functions of the affected channels.

One second task to be performed relies on understanding the reason behind the unreliability of the bow-tie method for inferring the effective geometric factor of P2, which is fundamental, so the data collected by this channel can be of any use. Ways to improve the inadequacy include a further study on the existence of a possible conversion factor CF_2, which was introduced in this work, or a re-arrangement of the channels.

Ideally, the data would benefit most from other methods of flux reconstruction, relying on machine learning techniques (e.g. as in [30]), so the form of the energy spectra does not have to be assumed a priori. The results of this work can serve as benchmark to construct alternative algorithms.

Finally, and to further characterize BERM, it is important to analyse its interaction with heavy ions. So far the behavior of the 5 heavy ion channels, as well as the data recorded by them, has not been analysed. Studying the response of the monitor to heavy ions and understand how their flux can be reconstructed from the raw data, will allow to make maximum use of the data provided by BERM.

Bibliography

[1] V. Mangano, M. Dósa, and M. e. a. Fränz, "Bepicolombo science investigations during cruise and flybys at the earth, venus and mercury." *Space Sci Rev*, vol. 217, no. 23, 2021.

[2] *Mercury's Dynamic Magnetosphere*, ser. Cambridge Planetary Science. Cambridge University Press, 2018, p. 461–496.

[3] R. A. Mewaldt *et al.*, "Proton, helium, and electron spectra during the large solar particle events of october–november 2003," *Journal of Geophysical Research: Space Physics*, vol. 110, no. A9, 2005. [Online]. Available: https://agupubs.onlinelibrary.wiley.com/doi/abs/10.1029/2005JA011038

[4] A. Milillo *et al.*, "Investigating mercury's environment with the two-spacecraft bepicolombo mission," *Space Science Review*, vol. 216, no. 93, 2020, comparative Magnetospheres.

[5] M. Pinto *et al.*, "The BepiColombo Radiation Monitor, BERM," *Space Science Reviews*, vol. 217, 2022.

[6] Efacec. [Online]. Available: https://www.efacec.pt/

[7] ESA. Bepicolombo mission. [Online]. Available: https://sci.esa.int/web/bepicolombo/home

[8] European space agency, mercury planetary orbiter - spacecraft. [Online]. Available: https://sci.esa.int/web/bepicolombo/-/48872-spacecraft

[9] European space agency, mercury magnetospheric orbiter - spacecraft. [Online]. Available: https://sci.esa.int/web/bepicolombo/-/49481-spacecraft

[10] J. Huovelin *et al.*, "Solar intensity x-ray and particle spectrometer sixs: Instrument design and first results," *Space Science Reviews*, vol. 216, pp. 94–136, 2020.

[11] Laboratório de instrumentação e física experimental de partículas. [Online]. Available: https://www.lip.pt/

[12] L. R. W. Y. S. K. Ness NF, Behannon KW, "Magnetic field observations near mercury: Preliminary results from mariner 10," *Science*, vol. 185, pp. 151–160, 1974.

[13] T. P. Armstrong, S. M. Krimigis, and L. J. Lanzerotti, "A reinterpretation of the reported energetic particle fluxes in the vicinity of mercury," *Journal of Geophysical Research (1896-1977)*, vol. 80, no. 28, pp. 4015–4017, 1975.

[14] A. B. Galvin *et al.*, "Solar wind composition: First results from soho and future expectations," *Bulletin of the American Astronomical Society*, vol. 28, p. 897, 1996.

[15] J. Sorensen, "Mercury environmental specification (part ii). bepicolombo definition study," *Space Environment and Effects Analysis Section ESA/ESTEC/TOS-EMA*, 2004.

[16] D. N. Baker *et al.*, "Intense energetic electron flux enhancements in mercury's magnetosphere: An integrated view with high-resolution observations from messenger," *Journal of Geophysical Research: Space Physics*, vol. 121, no. 3, pp. 2171–2184.

[17] G. Mason *et al.*, "The Heavy-Ion Compositional Signature in 3He-rich Solar Particle Events," , vol. 303, p. 849, Apr. 1986.

[18] D. V. Reames, "Magnetic topology of impulsive and gradual solar energetic particle events," *The Astrophysical Journal*, vol. 571, no. 1, pp. L63–L66, may 2002. [Online]. Available: https://doi.org/10.1086/341149

[19] B. T. Tsurutani *et al.*, "The extreme magnetic storm of 1–2 september 1859," *Journal of Geophysical Research: Space Physics*, vol. 108, no. A7, 2003. [Online]. Available: https://agupubs.onlinelibrary.wiley.com/doi/abs/10.1029/2002JA009504

[20] H. Moraal, "Cosmic-ray modulation equations," *Space Science Review*, vol. 176, pp. 299–319, 2013.

[21] R. Vainio *et al.*, "Dynamics of the earth's particle radiation environment," *Space Science Reviews*, vol. 147, pp. 187–231, 2009.

[22] J. Simpson *et al.*, "Electrons and protons accelerated in mercury's magnetic field," *Science*, vol. 185, no. 4146, pp. 160–166, 1974.

[23] J. H. Eraker and J. A. Simpson, "Acceleration of charged particles in mercury's magnetosphere," *Journal of Geophysical Research: Space Physics*, vol. 91, no. A9, pp. 9973–9993, 1986.

[24] Cern. (2020) Geant4 physics reference manual release 10.7, page 157. [Online]. Available: https://geant4-userdoc.web.cern.ch/UsersGuides/PhysicsReferenceManual/fo/PhysicsReferenceManual.pdf

[25] M. Pinto and P. Gonçalves, "Guimesh: A tool to import step geometries into geant4 via gdml," *Computer Physics Communications*, vol. 239, pp. 150–156, 2019. [Online]. Available: https://www.sciencedirect.com/science/article/pii/S0010465519300438

[26] J. Van Allen *et al.*, "The magnetosphere of Jupiter as observed with Pioneer 10: 1. Instrument and principal findings," , vol. 79, no. 25, p. 3559, Jan. 1974.

[27] P. Oleynik, "Particle observations in near-earth space: Design and verification of particle instruments for cubesat experiments," Ph.D. dissertation, University of Turku, 2021.

[28] A. Boudouridis *et al.*, "Development of a bowtie inversion technique for real-time processing of the goes-16/-17 seiss mps-hi electron channels," *Space Weather*, vol. 18, no. 4, p. e2019SW002403, 2020.

[29] H. Zhao *et al.*, "Characterization and evolution of radiation belt electron energy spectra based on the van allen probes measurements," *Journal of Geophysical Research: Space Physics*, vol. 124, no. 6, pp. 4217–4232, 2019. [Online]. Available: https://agupubs.onlinelibrary.wiley.com/doi/abs/10.1029/2019JA026697

[30] Aminalragia-Giamini, S., Papadimitriou, C., Sandberg, I., Tsigkanos, A., Jiggens, P., Evans, H., Rodgers, D., and Daglis, I. A., "Artificial intelligence unfolding for space radiation monitor data," *J. Space Weather Space Clim.*, vol. 8, p. A50, 2018. [Online]. Available: https://doi.org/10.1051/swsc/2018041

A

Complementary Figures

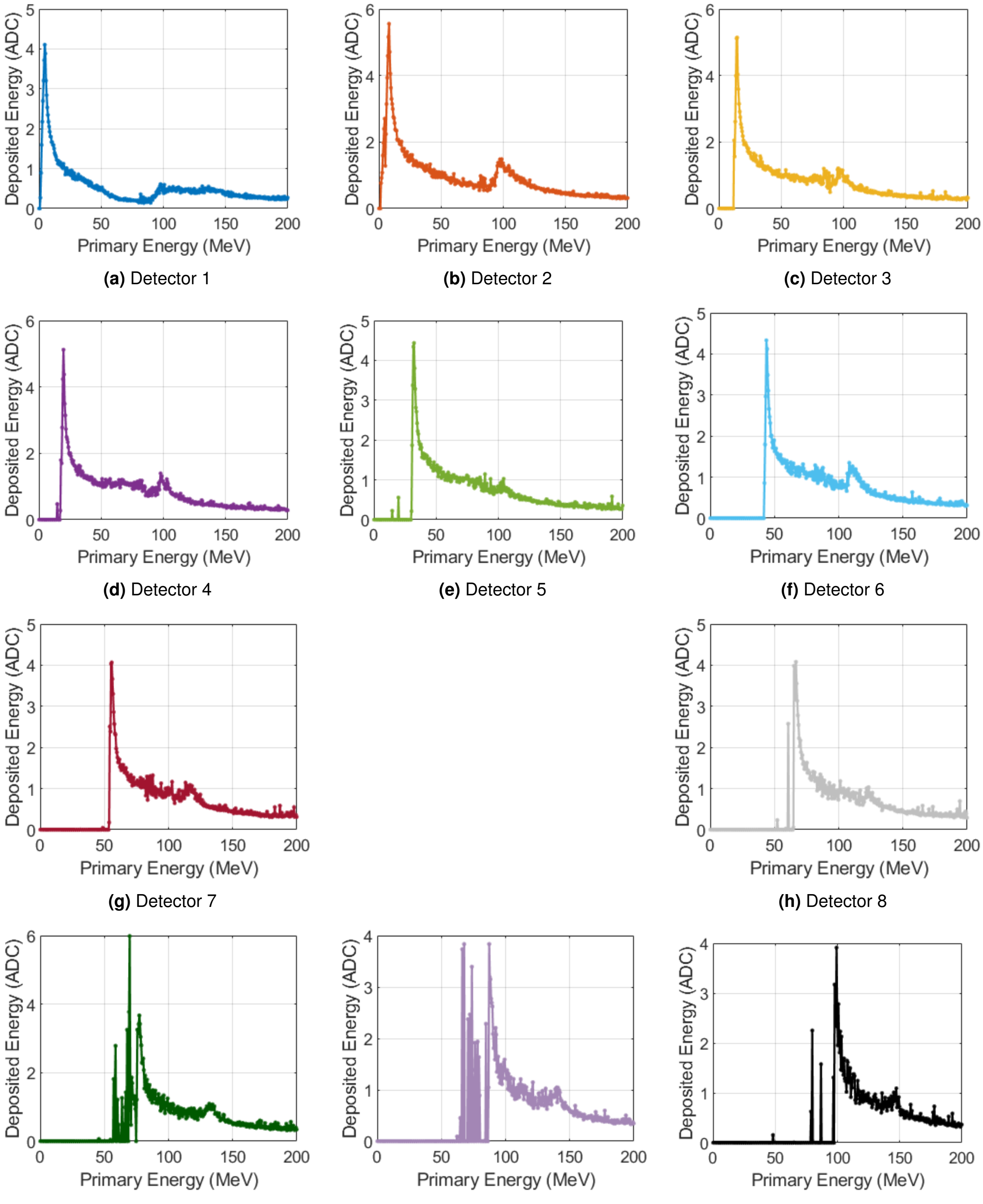

(a) Detector 1
(b) Detector 2
(c) Detector 3
(d) Detector 4
(e) Detector 5
(f) Detector 6
(g) Detector 7
(h) Detector 8
(i) Detector 9
(j) Detector 10
(k) Detector 11

Figure A.1: Energy deposited in the detectors depending on the initial energy of the incident proton.